THE GEOLOGICAL SOCIETY OF AMERICA®

Distributed north-vergent shear and flattening through Greater and Tethyan Himalayan rocks: Insights from metamorphic and strain data from the Dang Chu region, central Bhutan

Sean P. Long[1,*], Stacia M. Gordon[2], and Emmanuel Soignard[3]
[1]SCHOOL OF THE ENVIRONMENT, WASHINGTON STATE UNIVERSITY, PULLMAN, WASHINGTON 99164, USA
[2]DEPARTMENT OF GEOLOGICAL SCIENCES AND ENGINEERING, UNIVERSITY OF NEVADA, RENO, NEVADA, 89557, USA
[3]LEROY EYRING CENTER FOR SOLID STATE SCIENCE, ARIZONA STATE UNIVERSITY, TEMPE, ARIZONA 85287, USA

ABSTRACT

In several places in the Himalaya, there are debates over the location of and defining criteria for the South Tibetan detachment (STD) system. Here, we attempt to resolve this debate in central Bhutan by interpreting temperature, pressure, finite strain, and shear-sense data from an 11-km-thick structural transect through the Dang Chu region. Raman spectroscopy on carbonaceous material and garnet-biotite thermometry define a gradual, structurally upward decrease from 600–700 °C to 400–500 °C, and structural data indicate pure shear-dominant (W_m ≤0.4), layer-normal flattening strain and north-vergent shearing distributed through most of the section. Our data, when combined with published data from central Bhutan, define gradual, structurally upward cooling and an upright pressure gradient that is 1.2–2.4 times lithostatic distributed between 0 and 11 km above the Main Central thrust (MCT). Transport-parallel lengthening varies between ~20%–110% at 2–5 km above the MCT and between ~5%–55% at 5–11 km above the MCT, and north-vergent shearing is distributed between 2 and 11 km above the MCT. These data rule out the presence of a discrete, normal-sense shear zone and instead illustrate distributed structural thinning accommodated by north-vergent shearing. The strain data allow for ~85 km of distributed north-vergent displacement, which may be related to differential southward transport during MCT emplacement. Alternatively, distributed shear may have been translated northward into the STD system in northern Bhutan. Timing constraints for shearing on the MCT and STD allow for both possibilities. Central Bhutan provides a case study for large-scale, distributed structural thinning, and highlights the diverse range of processes that accommodate tectonic denudation during orogenesis.

LITHOSPHERE; v. 9; no. 5; p. 774–795; GSA Data Repository Item 2017271 | Published online 14 July 2017 https://doi.org/10.1130/L655.1

1. INTRODUCTION

The structural and kinematic framework of an orogenic belt is the foundation upon which all interpretations of the processes that accommodate convergence are built. In the past two decades, arguably no other orogenic system has seen more debate over its basic structural framework than the Himalaya (e.g., Grujic et al., 1996; Robinson et al., 2006; Webb et al., 2007; Kohn, 2008; Searle et al., 2008; Long and McQuarrie, 2010; Larson and Cottle, 2014; He et al., 2015; Larson et al., 2015). The Himalaya is dominated by exposures of complexly deformed metamorphic rocks, and the criteria used to define major shear zones within these rocks differ widely among studies (e.g., Harrison et al., 1997; DeCelles et al., 2000; Martin et al., 2005; Searle et al., 2008; Martin, 2016). One of the key debates is over the style, location, offset magnitude, and structural significance of the normal-sense South Tibetan detachment (STD) system, a structure that features prominently in all models of Himalayan evolution (e.g., Grujic et al., 1996; Beaumont et al., 2001; Robinson et al., 2003; Webb et al., 2007; Kohn, 2008). Understanding the role that the STD system has played in the exhumation of mid-crustal rocks is critical for assessing the applicability of tectonic models proposed for Himalayan evolution, including models that invoke large-scale channelized flow (e.g., Grujic et al., 1996; Beaumont et al., 2001; Godin et al., 2006) and models that propose that the Himalaya evolved as an orogenic wedge that grew dominantly through duplexing (e.g., Kohn, 2008; He et al., 2015). Analysis of the geometry and offset magnitude of the STD also has implications for the pre-collisional stratigraphic architecture of the Himalaya, including for evaluation of models that propose pre-collisional stratigraphic continuity of the northern Indian margin (e.g., Myrow et al., 2009; McQuarrie et al., 2013), versus models that propose pre-collisional geographic separation of rock packages that are now juxtaposed in the Himalaya (e.g., van Hinsbergen et al., 2012).

The STD was originally defined as a system of orogen-parallel, north-vergent normal faults and shear zones that approximately demarcate the northern boundary of the Himalayan orogen with the Tibetan plateau (Fig. 1A) (e.g., Burg et al., 1984; Burchfiel et al., 1992; Hodges et al., 1992). More recently, several exposures of structures correlated with the STD system have been mapped farther south within the orogen, although in several places, most notably Nepal and Bhutan, the location, kinematics, and existence of these structures are debated (e.g., Grujic et al., 2002; Robinson et al., 2003, 2006; Long and McQuarrie, 2010; Corrie

*sean.p.long@wsu.edu

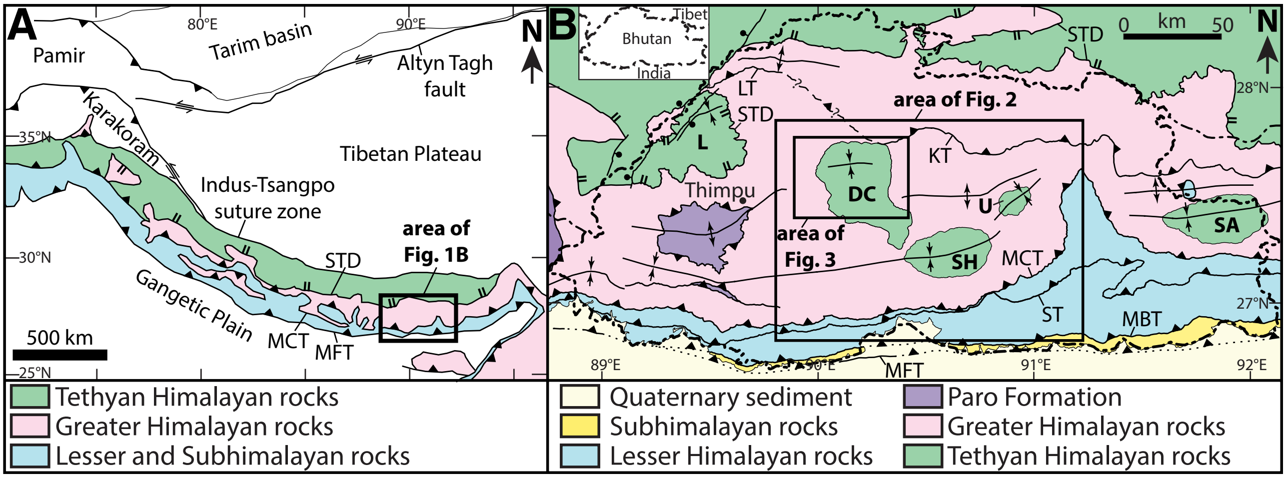

Figure 1. (A) Generalized geologic map of the Himalayan-Tibetan orogen, showing tectonostratigraphic divisions of the Himalayan thrust belt (simplified from Yin, 2006). (B) Simplified geologic map of Bhutan (modified from Long et al., 2012, and McQuarrie et al., 2013). Structure abbreviations: MFT—Main Frontal thrust; MBT—Main Boundary thrust; ST—Shumar thrust; MCT—Main Central thrust; STD—South Tibetan detachment; K—Kakthang thrust; LT—Laya thrust. Tethyan Himalayan exposure abbreviations: L—Lingshi; DC—Dang Chu; SH—Shemgang; U—Ura; SA—Sakteng.

et al., 2012; Antolín et al., 2013; He et al., 2015, 2016; Khanal et al., 2015; Soucy La Roche et al., 2016). In Bhutan, as many as five isolated, southern exposures of north-vergent shear zones correlated with the STD have been mapped (Fig. 1B). In central Bhutan, there has been significant disagreement over the location of these southern exposures of the STD, with multiple studies mapping it at a different structural level (Fig. 2) (Grujic et al., 2002, 2011; Kellett et al., 2009; Long et al., 2011d; Cooper et al., 2013; Greenwood et al., 2016), and other studies interpreting the rocks in this region to reflect a thick zone of distributed north-vergent shearing, rather than a discrete shear zone (Long and McQuarrie, 2010; Corrie et al., 2012). Much of this disagreement can be attributed to differing interpretations of the tectonostratigraphic affinity of rocks in central Bhutan, specifically whether they are part of the Greater Himalayan (GH) or Tethyan Himalayan (TH) units, which are traditionally mapped in the footwall and hanging wall of the STD, respectively. In addition, different studies utilize varying criteria to define the STD, including qualitative assessment of metamorphic grade, deformation conditions, and strain magnitude (Grujic et al., 2002; Greenwood et al., 2016), and trends in metamorphic temperature (Cooper et al., 2013).

In this study, we attempt to reconcile these disparate models for the tectonostratigraphy of central Bhutan by integrating temperature (T), pressure (P), finite strain, and shear-sense data distributed through an 11-km-thick structural transect along the Dang Chu in west-central Bhutan. This transect has been interpreted in multiple studies to contain an exposure of the STD, albeit at different structural levels. Our data are integrated with published T, P, strain, and shear-sense data from central Bhutan in order to define trends with structural distance above the Main Central thrust (MCT). We then explore the implications of these data for the structural evolution of Himalayan deformation in Bhutan.

2. HIMALAYAN GEOLOGIC BACKGROUND

The Himalayan-Tibetan orogen has formed in response to Cenozoic collision and continued convergence between India and Asia (e.g., Gansser, 1964; Yin and Harrison, 2000). The southern part of the orogen consists of the south-vergent Himalayan thrust belt (Fig. 1A), which deforms sedimentary, metasedimentary, and igneous rocks native to Greater India (e.g., Powell and Conaghan, 1973; Mattauer, 1986; DeCelles et al., 2002; Yin, 2006). The thrust belt has been divided into four tectonostratigraphic zones, which in most places are separated by first-order structures that can be correlated across the width of the orogen. In the south, the Main Frontal thrust places Neogene sedimentary rocks of the Subhimalayan zone over modern foreland basin sediments. To the north, Lesser Himalayan rocks are juxtaposed atop the Subhimalayan rocks by the Main Boundary thrust. The Lesser Himalayan zone is dominated by Precambrian to Paleozoic, greenschist-facies sedimentary rocks, which are deformed into a south-vergent thrust belt characterized by large duplex systems (e.g., Robinson et al., 2006; Bhattacharyya and Mitra, 2009; Long et al., 2011a; Webb, 2013; He et al., 2015). Farther north, the Main Central thrust (MCT) places high-grade (typically upper amphibolite–facies and migmatitic) metasedimentary and metaigneous GH rocks over Lesser Himalayan rocks, creating an inverted metamorphic field gradient (e.g., LeFort, 1975; Harrison et al., 1997; Kohn, 2014). To the north, Paleozoic to Mesozoic, greenschist-facies to unmetamorphosed sedimentary rocks of the TH zone overlie GH rocks.

In most places, TH rocks lie structurally above GH rocks across the STD system (e.g., Burchfiel et al., 1992). However, in several localities, the contact relationship between GH and TH rocks has been debated, with some interpreting it as conformable, without any metamorphic discontinuity (e.g., Gansser, 1964, 1983; Robinson et al., 2006; Long and McQuarrie, 2010; Corrie et al., 2012) and others interpreting it as a discrete, north-vergent shear zone (e.g., Godin et al., 1999; Antolín et al., 2013; He et al., 2015). For example, in the Annapurna region of northern Nepal, earlier studies mapped the GH-TH contact as conformable (e.g., Gansser, 1964; Bordet et al., 1971; Colchen et al., 1981), while later studies interpreted it as a normal-sense shear zone (Caby et al., 1983; Pêcher, 1991), which was later correlated with the STD system (Brown and Nazarchuk, 1993; Godin et al., 1999). Similarly, in the Almora-Dadeldhura and Kathmandu klippen in western and central Nepal, several have mapped the GH-TH contact as conformable (Stocklin, 1980; Upreti and LeFort, 1999; DeCelles et al., 2001; Johnson et al., 2001; Gehrels et al., 2003, 2006a, 2006b; Robinson et al., 2006), while others have interpreted this contact as a shear zone correlated with the STD system (Webb et al., 2011; Antolín et al., 2013; He et al., 2015, 2016; Soucy La Roche et al., 2016). Central Bhutan,

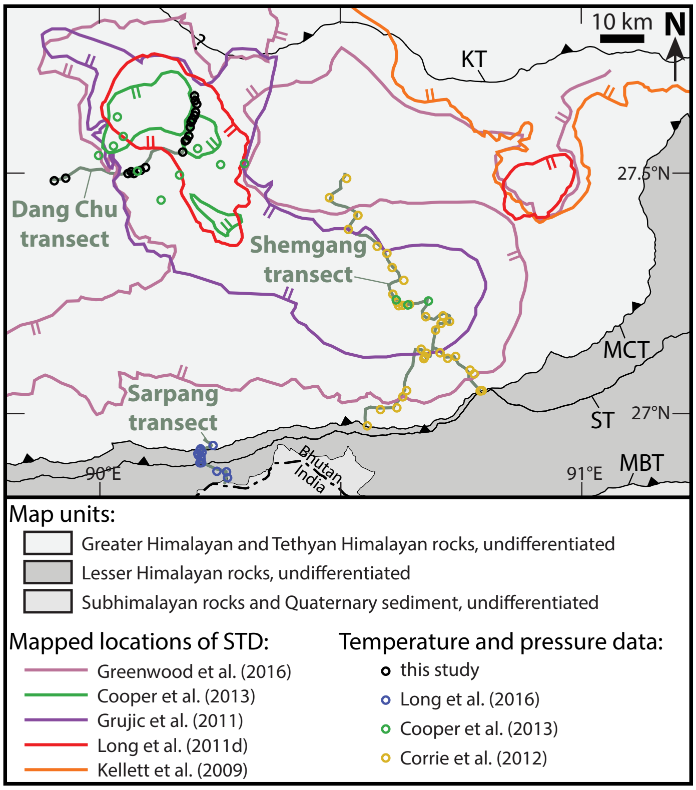

Figure 2. Simplified geologic map of central Bhutan, showing variation in the mapped locations of the South Tibetan detachment (STD) in previous studies, and locations of P-T samples used in the data compilation. Mapping transects are labeled in gray. Structure abbreviations: MBT—Main Boundary thrust; ST—Shumar thrust; MCT—Main Central thrust; KT—Kakthang thrust.

another site of debate over the location, defining criteria, and presence or absence of the STD, is expanded upon below.

3. GREATER HIMALAYAN ROCKS, TETHYAN HIMALAYAN ROCKS, AND THE SOUTH TIBETAN DETACHMENT IN CENTRAL BHUTAN

Greater Himalayan rocks in Bhutan are dominated by upper amphibolite–facies orthogneiss and metasedimentary rocks, including paragneiss, schist, quartzite, marble, and calc-silicate (e.g., Gansser, 1983; Swapp and Hollister, 1991; Grujic et al., 1996; Davidson et al., 1997; Kellett et al., 2009, 2010; Long et al., 2011d; Warren et al., 2011). Greater Himalayan rocks in Bhutan have been divided into two structural levels, which are separated by the Kakthang and/or Laya thrusts in northern Bhutan (Fig. 1B) (Swapp and Hollister, 1991; Grujic et al., 2002, 2011; Warren et al., 2011, 2012). In northwestern Bhutan, Warren et al. (2011) showed that GH rocks above the Laya thrust attained eclogite- and granulite-facies conditions prior to their exhumation, whereas those below were deformed at upper amphibolite–facies conditions. In comparison, discrete P ± T inversions within an overall upright, upper amphibolite–facies P-T gradient at and above the Kakthang thrust in north-central and northeastern Bhutan have been interpreted to represent construction of the upper part of the GH section through ductile underplating along multiple shear zones (Zeiger et al., 2015; Agustsson et al., 2016).

The structurally lower portion of the GH is exposed between the MCT and the Kakthang or Laya thrust (Fig. 1B). Several researchers have mapped exposures of a north-vergent, ductile shear zone correlated with the STD system in central Bhutan. This shear zone is interpreted to separate underlying GH rocks from overlying rocks correlated with the TH zone and to project beneath the Kakthang thrust toward the north (Grujic et al., 2002; Kellett et al., 2009). However, there is disagreement over the interpreted affinities of rocks above and below the STD (i.e., the definition of "GH" versus "TH" rocks), the criteria that define the STD, its location (Fig. 2), whether it is a discrete structure or a diffuse shear zone, or whether it is present at all (e.g., Kellett et al., 2009; Long and McQuarrie, 2010; Corrie et al., 2012; Cooper et al., 2013; Greenwood et al., 2016). The following discussion presents a chronological review of the evolving interpretations of the tectonostratigraphy of central Bhutan.

In his pioneering work in Bhutan, Gansser (1983) mapped gneisses and metasedimentary rocks of the "Main Crystalline of the High Himalaya" (referred to here as GH rocks) above the MCT. Overlying these rocks, he mapped three isolated exposures of a metasedimentary unit correlated with the TH zone called the Chekha Formation, one surrounding the town of Shemgang, one along the Dang Chu, and one in the Lingshi region of northwest Bhutan (referred to here as the Shemgang, Dang Chu, and Lingshi exposures; Fig. 1B). The Chekha Formation consists of non-migmatitic, garnet- and locally staurolite-bearing quartzite, schist, marble, and calc-silicate, and is interpreted to be of lower metamorphic grade than underlying GH rocks. Within the Dang Chu and Lingshi exposures, Gansser (1983) also mapped isolated exposures of Paleozoic to Mesozoic metasedimentary TH rocks, which overlie the Chekha Formation. Gansser (1983) described the upper and lower contacts of the Chekha Formation as conformable and thus did not map either contact as a structure. On his metamorphic-facies map, Gansser (1983) shows a gradual, structurally upward decrease in metamorphic grade from upper amphibolite facies at the MCT, to lower amphibolite facies higher in the GH section, to upper greenschist facies within the Chekha Formation, to lower greenschist facies within the Paleozoic–Mesozoic TH rocks in the Dang Chu and Lingshi exposures.

After recognition of the STD system in Tibet (Burchfiel et al., 1992), Edwards et al. (1996) hypothesized that the Paleozoic–Mesozoic TH rocks in the Lingshi and Dang Chu exposures may be klippen underlain by the STD. Grujic et al. (2002) were the first to present field evidence for north-vergent shearing in rocks above the MCT in central Bhutan, and they interpreted shear zones correlated with the STD at the base of five isolated Chekha Formation exposures (the Lingshi, Dang Chu, and Shemgang exposures in western and central Bhutan and the Ura and Sakteng exposures in eastern Bhutan; Fig. 1B). This interpretation was based on evidence for north-vergent shearing and an upsection decrease in metamorphic grade and apparent deformation conditions, with melt-present deformation at amphibolite-facies conditions below the STD and deformation at greenschist-facies conditions above (Grujic et al., 2002).

Following this, Kellett et al. (2009) differentiated the main exposure of the STD in northernmost Bhutan (the "inner STD") from the exposures of the STD underlying the Chekha Formation farther to the south (the "outer STD"). The outer STD was described as a ductile shear zone that was active between ca. 22–24 Ma, the timing of youngest prograde monazite growth in the footwall, until at least ca. 16 Ma, the timing of crystallization of weakly deformed granite in the hanging wall (Kellett et al., 2009). In comparison, the inner STD consists of a lower brittle-ductile fault that places metasedimentary TH rocks over GH rocks and an upper brittle fault that places unmetamorphosed Paleozoic TH rocks over metasedimentary TH rocks (Burchfiel et al., 1992; Kellett et al., 2009). The lower fault of the inner STD was active until at least ca. 11–12 Ma, the timing of crystallization of deformed granite in its footwall (Edwards and Harrison, 1997; Wu et al., 1998; Kellett et al., 2009). The inner STD is hypothesized to be contemporary with ca. 11–15 Ma south-vergent shearing on the Kakthang thrust (Grujic et al., 2002; Kellett et al., 2009); therefore, the outer STD was interpreted to represent an older segment that was abandoned at ca. 16 Ma, when deformation shifted northward to the Kakthang thrust and inner STD (Kellett et al., 2009, 2010).

Long and McQuarrie (2010) and Corrie et al. (2012) argued that the STD is not present within the Shemgang exposure. This interpretation was based on: (1) observation of lithologies with similar mineral assemblages above and below the Chekha Formation–GH contact; (2) north-vergent shearing distributed from ~2 km above the MCT through the full ~10-km-thick package of overlying GH and TH rocks; (3) finite strain data that indicate bulk flattening of all rocks above the MCT (Long et al., 2011c); and (4) uniform, upright field gradients of 20 ± 2 °C/km and 0.57 ± 0.08 kbar/km (approximately two times lithostatic) above the MCT, with no P or T discontinuities observed below, at, or above the base of the Chekha Formation (Corrie et al., 2012). The super-lithostatic pressure gradient was interpreted to indicate ~50% post-peak metamorphic flattening, accommodated by the distributed, north-vergent shearing.

Following this, several studies presented differing map patterns for the STD in central Bhutan (Fig. 2); these patterns are largely based on differences in how the Chekha Formation is defined and mapped. Kellett et al. (2009, 2010) extended the map pattern of the STD to the east and west of the Ura exposure, by including staurolite-bearing metasedimentary rocks mapped by Bhargava (1995) as the Naspe Formation as part of the Chekha Formation. Long et al. (2011d) mapped the STD at the Dang Chu and Ura exposures, with the map patterns of the Chekha Formation largely based on the mapping of Gansser (1983) and Grujic et al. (2002), respectively. Grujic et al. (2011) mapped a single, extensive exposure of the Chekha Formation soled by the STD, which connects the regions originally mapped separately as the Dang Chu and Shemgang exposures.

More recently, Cooper et al. (2013) proposed significant changes to the map pattern of the STD based on Raman spectroscopy of carbonaceous material (RSCM) thermometry. They obtained temperatures of ~500–600 °C from GH rocks and the Chekha Formation in the Dang Chu, Shemgang, and Ura exposures, and cooler temperatures of ~400–500 °C from Paleozoic TH rocks overlying the Chekha Formation in the Dang Chu exposure. Based on these data, they interpreted that the basal contact of the Chekha Formation is not a shear zone and therefore that the STD is not present in the Ura and Shemgang exposures; however, they interpreted that the STD is present in the Dang Chu exposure but mapped it at the contact between the Chekha Formation and overlying Paleozoic TH rocks (Fig. 2).

The most recent study in central Bhutan (Greenwood et al., 2016) presented a significant revision to the tectonostratigraphy, as a result of assignment of a ~100-km-wide, continuous region of lower amphibolite– to upper greenschist–facies metasedimentary rocks to TH affinity. In south-central Bhutan, this included rocks that Gansser (1983) originally mapped as part of the GH section (the Paro metasediments). Greenwood et al. (2016) interpreted that a discrete (~200–300-m-thick), north-vergent ductile STD zone bounds these TH rocks everywhere at their base (Fig. 2), which shifted the trace of the STD southward and lowered its structural level to within ~2 km above the MCT.

4. TECTONOSTRATIGRAPHY OF THE DANG CHU TRANSECT

The structural interpretations summarized above make claims that can be tested through analysis of trends in metamorphic conditions, microstructural deformation processes, finite strain magnitudes, and kinematics with structural distance. To accomplish this, we examined a transect through the Dang Chu exposure in west-central Bhutan (Figs. 1 and 3). Several studies have interpreted that this transect contains an exposure of the STD, albeit at varying structural levels (Grujic et al., 2011; Long et al., 2011d; Cooper et al., 2013; Greenwood et al., 2016).

We performed geologic mapping along an east-trending road east of Wangdue Phodrang, and a north-trending road north of Pele La (Fig. 3). The northern end of our transect crosses the axis of a regional-scale, east-trending syncline (Gansser, 1983; Gokul, 1983; Bhargava, 1995). Fifty-three outcrops were examined, with samples collected and thin sections made from 37 of these localities. Rocks at all localities exhibit a penetrative, macroscopic foliation, which typically dips toward the north or northeast (Fig. 3). Mineral-stretching lineations were observed in most outcrops and typically plunge approximately northward. Crenulation cleavage was also observed in several outcrops and typically trends approximately east-west.

Structural thicknesses were measured by projecting the apparent dip of foliation measurements onto a cross section (Fig. 4). Thicknesses were measured normal to foliation and are rounded to the nearest 10 m. The field stops and sample localities are projected onto a tectonostratigraphic column (Fig. 5), with structural distance listed relative to the base of the Chekha Formation. The transect encompasses a total thickness of 11,000 m, ranging from 5700 m below to 5300 m above the base of the Chekha Formation. On average, stops below, within, and above the Chekha Formation are spaced ~350 m, ~100 m, and ~250 m apart, respectively (Fig. 5). Lithologies on the Dang Chu transect are described below from structurally low to high.

4.1 Greater Himalayan Rocks

Between −5700 and −3050 m, migmatitic, sillimanite- and garnet-bearing paragneiss is interlayered with schist and calc-silicate. These rocks are mapped as the GH lower metasedimentary unit (GHlml) after Long et al. (2011d). Between −3050 and −2125 m, migmatitic orthogneiss is dominant and is interlayered with migmatitic, sillimanite- and garnet-bearing paragneiss; this interval is mapped as the GH orthogneiss unit (GHlo; Long et al., 2011d). In portions of this unit, the volume percentage of leucocratic material approaches ~40% (Fig. 6A). Between −2125 and 0 m, migmatitic, garnet-bearing paragneiss is observed, with the volume percentage of leucocratic material locally up to ~30% (Fig. 6B). This interval is mapped as the GH upper metasedimentary unit (GHlmu; Long et al., 2011d). GH rocks are intruded by deformed (stops 78 and 105) and undeformed (stop 110) leucogranite, which ranges from m-scale dikes to ~100–200-m-thick plutons (Fig. 5).

4.2 Chekha Formation

We map the base of the Chekha Formation at a structurally upward lithologic transition from paragneiss (stop 112) to fine-grained schist (stop 131), which is at a similar location to the mapping of Grujic et al. (2011) and Greenwood et al. (2016). This transition corresponds with the structurally highest position of gneissic banding and in situ partial melt observed on the transect. The basal 100 m of the Chekha Formation consists of garnet- and sillimanite-bearing schist. Above this, between +100 and +1350 m, the Chekha Formation consists of medium- to dark-gray phyllite (Fig. 6C) and fine-grained, garnet-bearing schist, which is interlayered with medium-gray, micaceous, locally garnet-bearing quartzite (Fig. 6E) and tan, pure, cliff-forming quartzite. Sillimanite is observed as high as +700 m (Figs. 5 and 6D). Weakly deformed to undeformed leucogranite is observed through this interval and ranges in size from ~100–200-m-thick intrusive bodies between 0 and +1000 m to m-scale dikes between +1200 and +1350 m (Fig. 6E). Between +1350 and +2200 m, the Chekha Formation is dominated by green, tan, and gray marble (Fig. 6F), which is interlayered with micaceous quartzite, phyllite, and

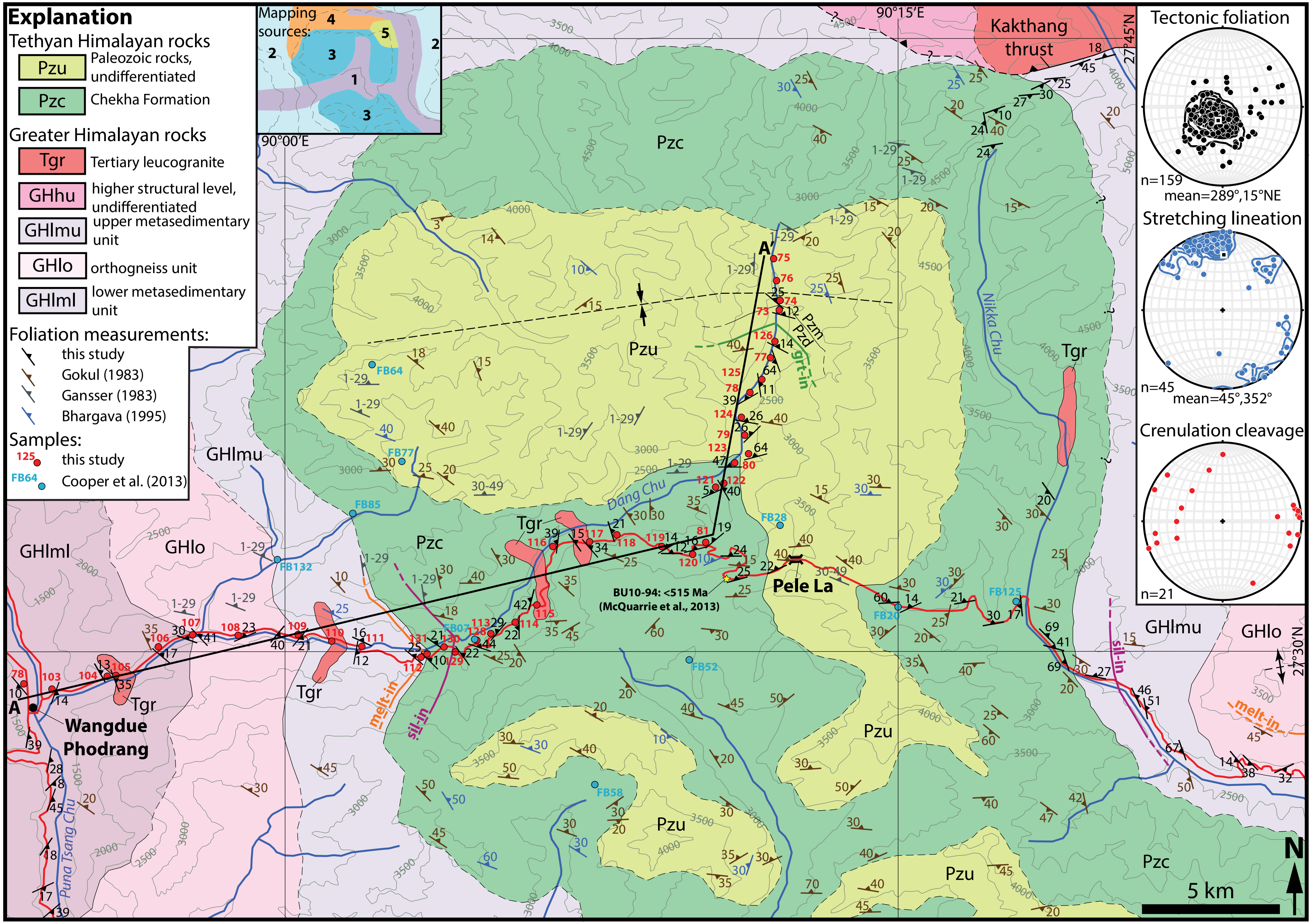

Figure 3. Geologic map of the Dang Chu region. The thick black line shows the location of cross-section A–A′. The Deshichilling (Pzd) and Maneting (Pzm) Formations are included in unit Pzu. The inset on the right shows equal-area stereoplots of all measurements of tectonic foliation (poles to planes plotted), mineral-stretching lineation, and crenulation cleavage (generated using Stereonet 8; Allmendinger et al., 2011). The mean vector and 1σ confidence envelope for each stereoplot are shown with the black box and circle. Mapping sources include: 1—this study; 2—Long et al. (2011d); 3—Bhargava (1995); 4—Gansser (1983); 5—Gokul (1983).

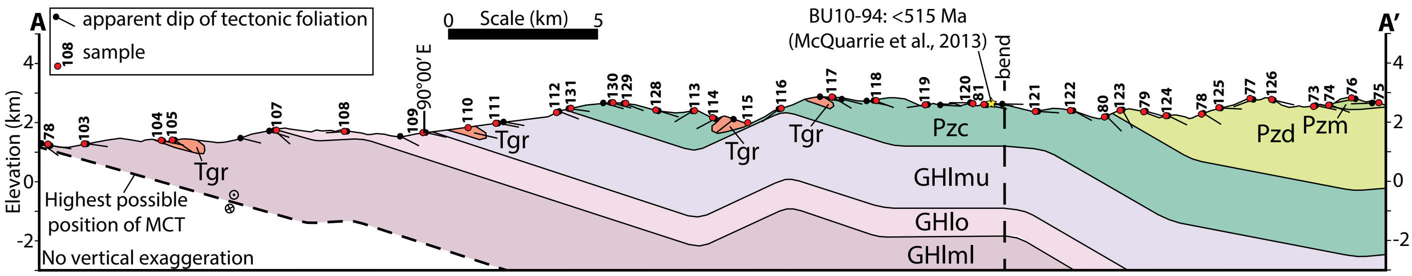

Figure 4. Cross section of the Dang Chu transect. An explanation of rock unit abbreviations is shown on Figure 3 (Pzd—Deshichilling Formation; Pzm—Maneting Formation). The structural level of the Main Central thrust (MCT) is supported by a dome mapped in Greater Himalayan (GH) rocks to the west (Long et al., 2011d); the dome exhumes GH rocks that are at equivalent structural levels to those exposed above the MCT ~60 km to the south. Thus, the MCT is interpreted to lie in the shallow subsurface.

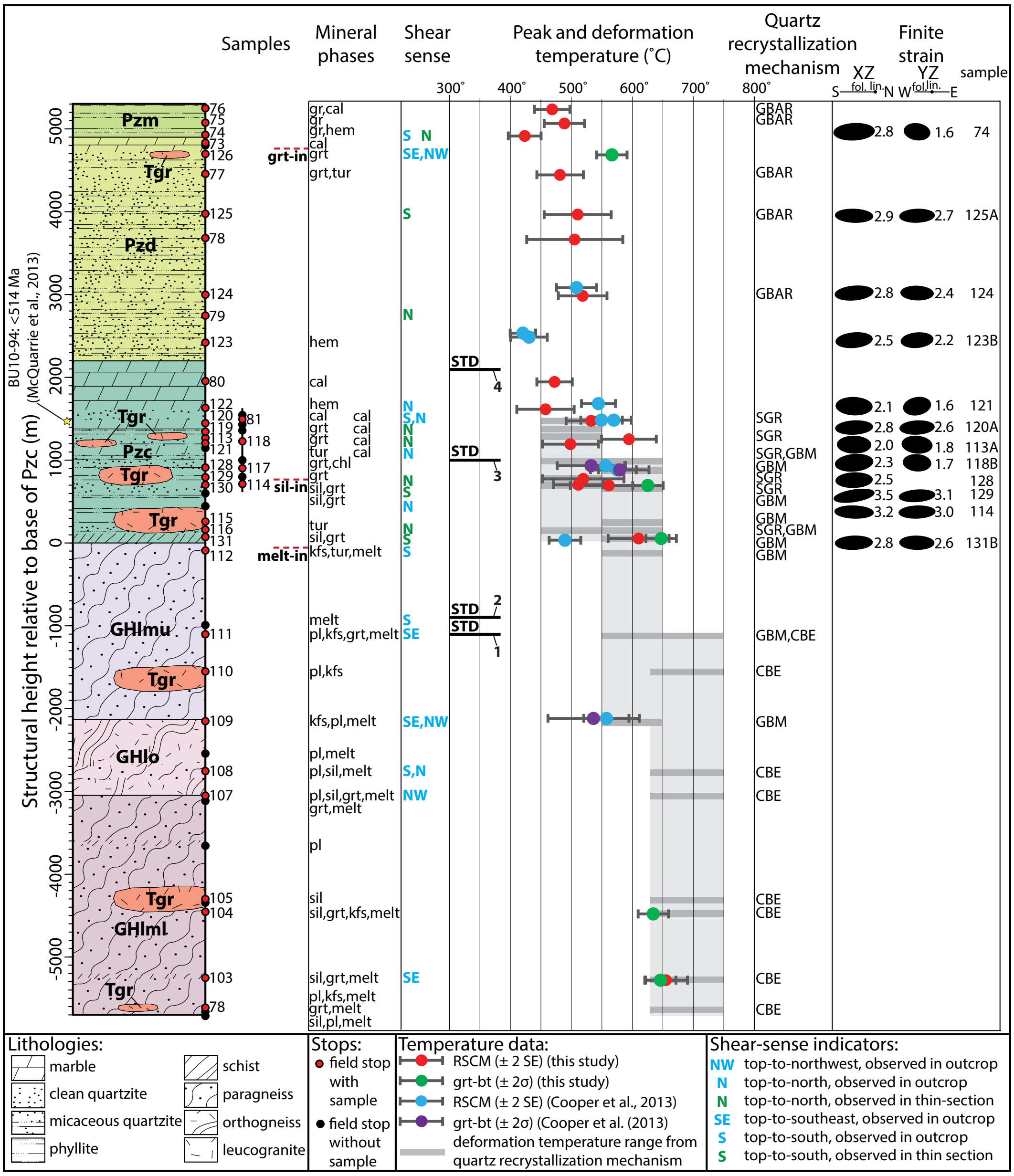

Figure 5. Tectonostratigraphic column of the Dang Chu transect, showing mineral phases (all samples also contain quartz, muscovite, and biotite; mineral abbreviations after Whitney and Evans, 2010), shear-sense, peak and deformation temperature, and finite strain data versus structural height (foliation-normal distance; measured from Fig. 4) relative to the basal contact of the Chekha Formation. SGR—subgrain rotation; GBM—grain boundary migration without chessboard extinction; CBE—grain boundary migration with chessboard extinction; GBAR—grain boundary area reduction. An explanation of rock unit abbreviations is shown on Figure 3. Bold numbers denote mapped locations of the South Tibetan detachment (STD) from the following studies: 1—Greenwood et al. (2016); 2—Grujic et al. (2011); 3—Long et al. (2011d); 4—Cooper et al. (2013).

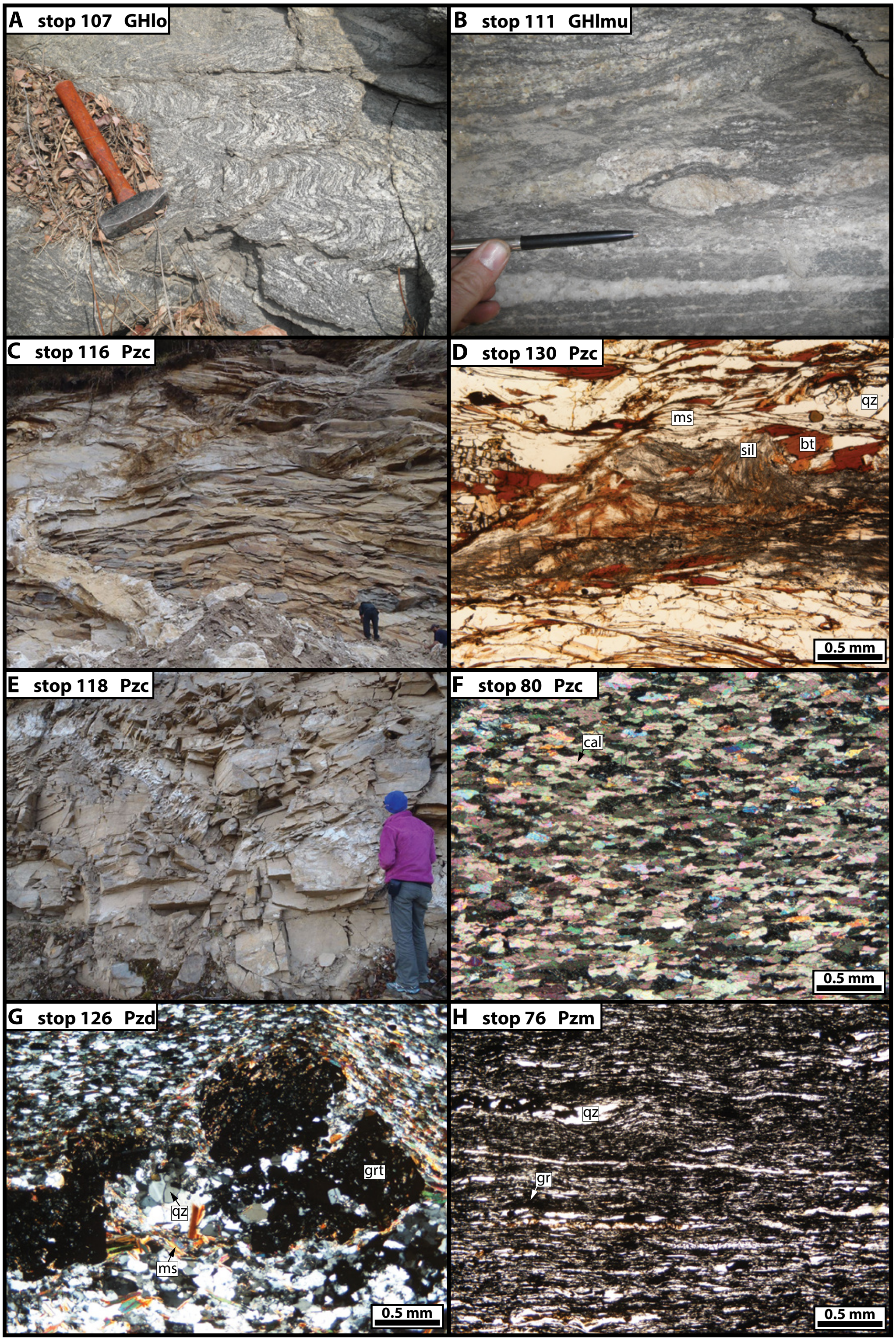

Figure 6. Photographs and photomicrographs illustrating representative lithologies and mineral assemblages observed on the Dang Chu transect, organized from structurally low to high (structural height relative to the basal Chekha Formation contact is listed below). (A) Migmatitic, feldspar-rich orthogneiss of unit GHlo (–3050 m). (B) Migmatitic, micaceous paragneiss of unit GHlmu (–1100 m). (C) Dark-gray phyllite of the basal Chekha Formation (+160 m) intruded by granite dikes. (D) Highest sillimanite observed on the transect, within Chekha Formation metapelite (+710 m; plane-polarized light [PPL]). (E) Gray quartzite of the Chekha Formation, intruded by a leucogranite dike (+1240 m). (F) Chekha Formation marble, exhibiting recrystallization and foliation-subparallel, shape-preferred elongation of calcite (+1960 m; cross-polarized light [XPL]). (G) Highest garnet porphyroblasts observed on the transect, within quartzite of the Deshichilling Formation (+4700 m; XPL). (H) Graphitic phyllite of the Maneting Formation (+5250 m; PPL). Mineral abbreviations are after Whitney and Evans (2010).

slate. Quartzite sampled from +1500 m (Figs. 3–5) yielded a ca. 515 Ma youngest detrital-zircon population (sample BU10-94 of McQuarrie et al., 2013), indicating a Cambrian maximum depositional age.

4.3 Deshichilling Formation

The interval between +2200 and +4900 m is dominated by gray, micaceous quartzite, which is interlayered with crenulated phyllite and white marble. After descriptions in Tangri and Pande (1995) and the mapping of Bhargava (1995), we mapped this unit as the Deshichilling Formation. Garnet porphyroblasts are observed in outcrops at +4700 and +4830 m, and these mark the structurally highest garnet observed on the transect (Fig. 6G). Boudinaged, m-scale, foliation-parallel leucogranites are observed near the top of the section.

4.4 Maneting Formation

Between +4900 and +5250 m, dark-gray, graphite-rich, crenulated phyllite is observed (Fig. 6H). After descriptions in Tangri and Pande (1995) and the mapping of Bhargava (1995), we mapped this unit as the Maneting Formation. The phyllite contains biotite and muscovite and locally contains up to ~50% graphite by volume (Fig. 6H).

5. TEMPERATURE DATA

The only published P-T data from the Dang Chu exposure come from Cooper et al. (2013), who obtained temperatures between ~450–600 °C (Raman spectroscopy on carbonaceous material [RSCM] thermometry; n = 7; garnet-biotite thermometry; n = 3) and pressures between ~4–7 kbar (garnet-biotite-muscovite-plagioclase barometry; n = 3) from GH rocks and the Chekha Formation, and temperatures between ~400–550 °C (RSCM thermometry; n = 3) from Paleozoic TH rocks overlying the Chekha Formation. Below, we supplement these data with 22 new quantitative temperature estimates and three new pressure estimates.

5.1. Quartz Recrystallization Microstructures

The microstructures of dynamically recrystallized quartz were analyzed in thin section to interpret dominant recrystallization mechanisms and to assess trends in deformation temperature with structural level (e.g., Stipp et al., 2002; Law, 2014). Approximate deformation temperature ranges corresponding to different recrystallization mechanisms and calibrated against examples taken from Himalayan rocks (Law, 2014) are utilized (Fig. 5). Four different recrystallization microstructures were observed (Fig. 7): (1) subgrain-rotation (SGR) recrystallization, which is indicated by equigranular, ~25–150 μm quartz neoblasts (defined here as visually distinct subgrains) (e.g., Poirier and Nicolas, 1975; White, 1977; Guillope and Poirier, 1979), and likely occurs at temperatures of ~450–550 °C (Law, 2014); (2) grain boundary migration (GBM) recrystallization, which is indicated by ~0.5–1.0 mm "amoeboid" quartz neoblasts with cuspate, interfingering boundaries (e.g., Guillope and Poirier, 1979; Urai et al., 1986), and likely occurs at temperatures of ~550–650 °C (Law, 2014); (3) chessboard extinction (CBE), which is typically observed within ≥0.5 mm amoeboid quartz neoblasts, is characterized by extinction domains that intersect at approximately right angles (e.g., Lister and Dornsiepen, 1982; Mainprice et al., 1986), and likely occurs at temperatures ≥~630 °C (Stipp et al., 2002); and (4) grain boundary area reduction (GBAR), which is characterized by polygonal quartz neoblasts with straight boundaries, with grain size often proportional to the width of the quartz-rich layer (e.g., Passchier and Trouw, 2005).

The Dang Chu transect rocks exhibit an overall pattern of quartz recrystallization at progressively cooler temperatures with increasing structural level (Fig. 5). Chessboard extinction is observed between −5620 and −1100 m (Figs. 7A and 7B), GBM recrystallization is observed between −2150 m and +910 m (Fig. 7C-E), and SGR recrystallization is observed between +160 and +1490 m (Figs. 7F and 7G). Grain boundary area reduction was only observed at the top of the transect, between +3000 and +5250 m (Fig. 7H).

5.2. Raman Spectroscopy on Carbonaceous Material (RSCM) Thermometry

Carbonaceous material (CM) is derived from metamorphism of organic matter and is common in metasedimentary rocks. The degree of structural organization of graphite bonds in CM is strongly temperature dependent and does not suffer significantly from retrograde reorganization; therefore, CM can be used to calculate metamorphic temperatures (e.g., Beyssac et al., 2002, 2003; Rahl et al., 2005; Aoya et al., 2010). Carbonaceous material was analyzed in situ from 17 samples of GH and TH metasedimentary rocks (Table 1). Measurements were made using a Raman spectrometer at Arizona State University (see Data Repository Item[1] for details on methodology and data from individual analyses). The laser was focused on CM situated beneath a transparent grain (typically quartz or calcite), after procedures outlined in Beyssac et al. (2003). Carbonaceous material was typically present as ~5–20 μm patches (Figs. 8A–8E). Examples of representative Raman spectra from each sample are shown on Figure 8F. We followed the methods of Rahl et al. (2005), in which the RSCM thermometer for rocks that achieved peak temperatures between ~100–740 °C was determined by measuring the height ratio (R1) and area ratio (R2) of four first-order Raman peaks (G, D1, D2, and D3) in the relative wavenumber range between 1200 and 1800 cm^{-1}. Mean peak temperatures of multiple measurements are shown on Table 1. Peak temperatures are reported with 2 standard errors, which take into account internal uncertainty and the external uncertainty from the Rahl et al. (2005) calibration (Table 1; e.g., Cooper et al., 2013).

Carbonaceous material from a quartzite sample from the GH lower metasedimentary unit (103A; −5300 m) yielded a temperature of 655 ± 35 °C. Nine samples of the Chekha Formation were analyzed from lithologies including schist, phyllite, slate, marble, and quartzite exposed between +70 and +1960 m. The resulting temperatures yielded a range between 610 ± 50 °C and 457 ± 47 °C, with a general structurally upward decrease in peak temperature, although the majority of analyses overlap within error (Fig. 5). Four Deshichilling Formation phyllite and quartzite samples (124, 78A, 125A, and 77AA), collected between +3000 and +4460 m, yielded similar temperatures (518 ± 40 °C; 505 ± 79 °C; 510 ± 55 °C; and 481 ± 38 °C, respectively). Three Maneting Formation phyllite samples (74A, 75, and 76), collected between +4900 and +5250 m, yielded temperatures of 423 ± 27 °C; 488 ± 33 °C; and 468 ± 29 °C, respectively.

5.3. Thermobarometry

Garnet-biotite temperatures were collected from five Dang Chu transect samples, including: (1) two GH samples, a micaceous quartzite (103A) collected at −5260 m and a migmatitic metapelite (104C) collected at −4460 m; (2) two Chekha Formation samples, a sillimanite-garnet

[1]GSA Data Repository Item 2017271, which includes details on thin sections, methodology, and supporting information for Raman spectroscopy on carbonaceous material thermometry, thermobarometry, finite strain analyses, and determination of kinematic vorticity, and compilation tables of published temperature, pressure, strain, and shear sense data from central Bhutan, is available at http://www.geosociety.org/datarepository/2017, or on request from editing@geosociety.org.

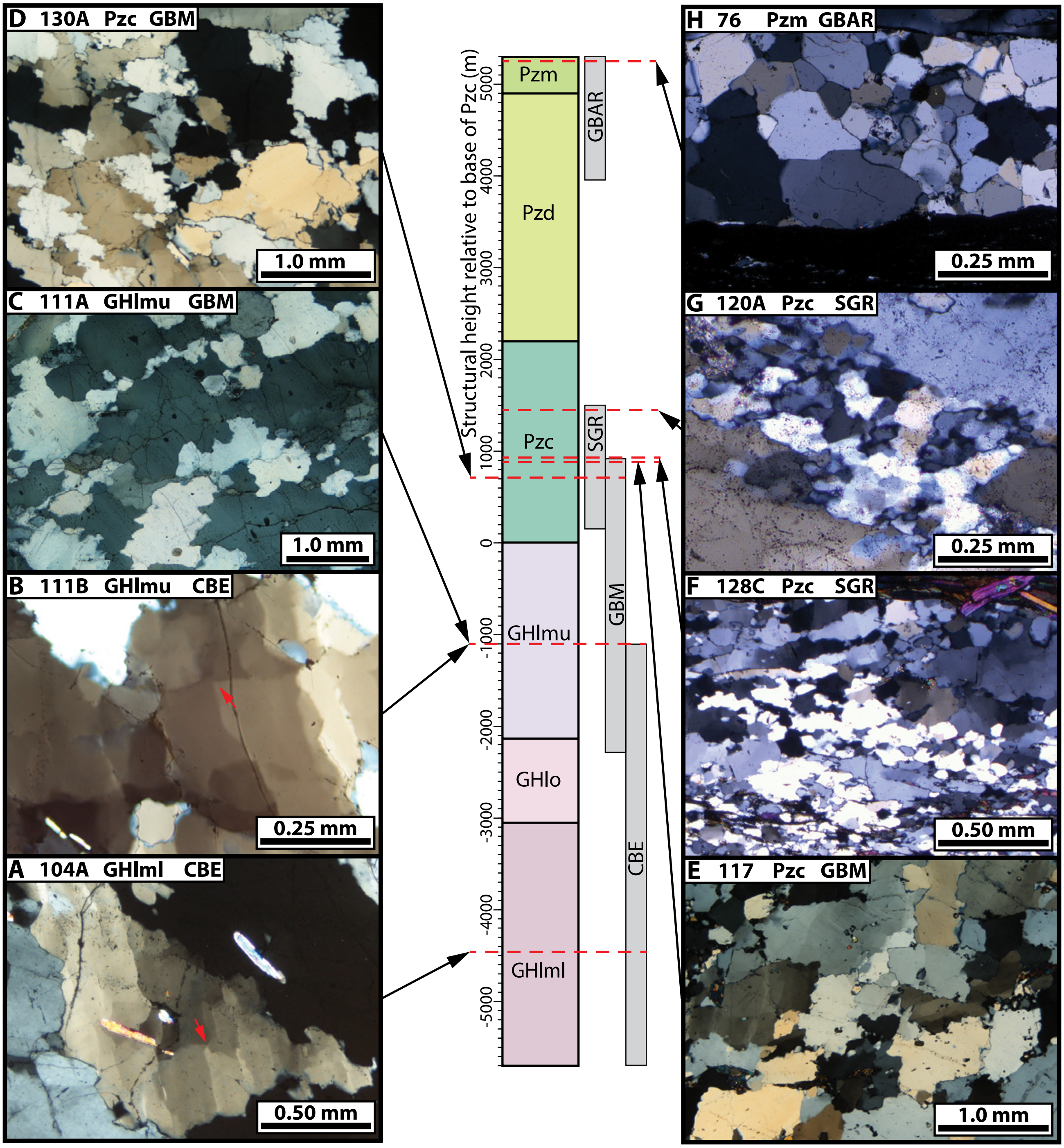

Figure 7. Photomicrographs illustrating representative quartz recrystallization microstructures observed on the Dang Chu transect, referenced to structural position on the tectonostratigraphic column. (A and B) Chessboard extinction (CBE) microstructure, characterized by ≥0.5 mm quartz neoblasts exhibiting multiple extinction domains that intersect at approximately right angles (red arrows). (C–E) Grain boundary migration (GBM) microstructure, characterized by ~0.5–1.0 mm, cuspate, interfingering, "amoeboid" quartz neoblasts. (F and G) Subgrain rotation (SGR) microstructure, defined by equigranular, ~25–150 µm quartz neoblasts. (H) Grain boundary area reduction (GBAR) microstructure, defined by polygonal neoblasts with straight boundaries. All photomicrographs were taken in XPL, on lineation-parallel thin sections. See Figure 3 for a guide to unit abbreviations.

TABLE 1. SUMMARY OF RSCM PEAK TEMPERATURE DETERMINATIONS FROM DANG CHU TRANSECT SAMPLES

Sample	Map unit	Lithology	Structural height (m)	R1		R2		Peak temperature (°C)			n
				Mean	1σ	Mean	1σ	Mean	1σ	2 SE	
76	Pzm	Phyllite	5250	0.386	0.082	0.356	0.043	468	27	29	15
75	Pzm	Phyllite	5080	0.246	0.302	0.070	0.053	488	37	33	14
74A	Pzm	Phyllite	4930	0.592	0.079	0.446	0.026	423	15	27	15
77AA	Pzd	Quartzite	4460	0.305	0.323	0.127	0.082	481	54	38	15
125A	Pzd	Phyllite	3980	0.181	0.065	0.265	0.103	510	93	55	15
78A	Pzd	Phyllitic quartzite	3680	0.207	0.273	0.207	0.175	505	134	79	13
124	Pzd	Phyllite	3000	0.216	0.101	0.266	0.073	518	51	40	13
80A	Pzc	Marble	1960	0.353	0.081	0.345	0.042	472	26	29	15
122	Pzc	Slate	1630	0.174	0.054	0.313	0.073	457	63	47	12
81	Pzc	Marble	1490	0.163	0.091	0.239	0.075	532	61	41	15
113E	Pzc	Phyllitic quartzite	1270	0.126	0.14	0.17	0.100	594	72	45	15
121	Pzc	Limestone	1210	0.277	0.135	0.287	0.104	498	74	46	15
129	Pzc	Phyllite	790	0.232	0.184	0.267	0.150	519	110	67	13
114	Pzc	Phyllite	720	0.264	0.145	0.285	0.090	511	61	41	15
130A	Pzc	Quartzite	710	0.110	0.197	0.072	0.100	561	86	63	10
131B	Pzc	Schist	70	0.098	0.148	0.100	0.104	610	84	50	15
103A	GHIml	Quartzite	–5260	0.037	0.022	0.088	0.048	655	44	35	15

Notes: R1, R2, and peak temperature values calculated using the calibration of Rahl et al. (2005). Internal variability in R1, R2, and peak temperature is indicated by 1σ uncertainty. Temperature is also reported with 2 standard errors (SE), calculated after Cooper et al. (2013), from quadratic addition of 1σ internal error and external error of ±50 °C from the Rahl et al. (2005) calibration, divided by the square root of the number of analyses (n). RSCM—Raman spectroscopy of carbonaceous material.

metapelite (131B) collected at +70 m and a fine-grained sillimanite-garnet metapelite (130B) collected at +710 m; and (3) a garnet-bearing siliceous gneiss of the Deshichilling Formation (126A), collected at +4700 m. The Deshichilling Formation sample contains the structurally highest occurrence of garnet observed on the transect. For all samples, the garnet-biotite calibration 5AV of Holdaway (2000) was used to calculate temperatures. In addition, pressures were determined from the three sillimanite-bearing samples via the Average P-T mode in THERMOCALC using the internally consistent data set of Holland and Powell (2011) (version 3.33; Powell and Holland, 1994). For the pressure calculations, temperatures were first calculated using the garnet-biotite exchange thermometer. In THERMOCALC, the X_{H_2O} content was systematically changed until the temperature overlapped with those calculated from the garnet-biotite thermometer (Table 2; e.g., Searle et al., 2003; Jessup et al., 2008; Agustsson et al., 2016).

Garnet, biotite, muscovite, and plagioclase were analyzed using a JEOL 8500F electron microprobe at Washington State University (see Data Repository Item for details on methodology). As garnet in most of the samples showed evidence for resorption and retrogressive diffusion, the lowest Fe/Fe + Mg and Mn compositions were used for the P-T calculations. For samples with evidence of retrogression effects, this corresponded to the near-rim of the garnet, whereas the rim was used for those samples that preserved their growth zoning. The other phases were not typically chemically zoned, and representative analyses of the rims of matrix grains were paired with the garnet. Activities of all phases were calculated using the program AX2 (Holland and Powell, 2003). The results are reported in Figure 9 and Table 2. For the garnet-biotite temperatures, errors are estimated at ±25 °C (2σ; Holdaway, 2000). Additional details on the methodology and phase chemistry of each sample are reported in the Data Repository Item.

The GH samples yielded nearly identical garnet-biotite temperatures of 646 ± 25 °C for the structurally lower 103A and 634 ± 25 °C for the higher 104C. Metapelite sample 104C yielded a pressure of 6.9 ± 1.2 kbar (1σ). In comparison, the Chekha Formation metapelite samples revealed similar temperatures and pressures: 647 ± 25 °C and 7.2 ± 1.2 kbar for the structurally lower 131B versus 625 ± 25 °C and 6.3 ± 1.1 kbar for the higher sample 130B. The Deshichilling Formation siliceous gneiss sample (126A) yielded a garnet-biotite temperature of 566 ± 25 °C. In comparing thermometers, the RSCM temperatures are generally consistent with the garnet-biotite temperatures. For example, samples 103A (655 ± 35 °C) and 131B (610 ± 50 °C) overlap within error with the garnet-biotite temperatures, and the RSCM temperature for sample 130A (561 ± 63 °C) overlaps within error with the garnet-biotite temperature of sample 130B, which was collected from the same outcrop. The similarity between the garnet-biotite and RSCM temperatures argues that they are likely recording the conditions of near-peak metamorphism.

5.4. Summary of Temperature with Structural Distance

Temperatures collected from this study and from Cooper et al. (2013) overlap within error with the quartz deformation temperature ranges (Fig. 5); therefore, we interpret that quartz recrystallization occurred while the rocks were at or near peak temperature. Samples between ~5.5–4.5 km below the base of the Chekha Formation yielded temperatures of ~625–675 °C, and Cooper et al. (2013) obtained temperatures of ~475–625 °C at ~2.0 km below the same contact. The Chekha Formation shows more variable results, with rocks from the basal 1.2 km yielding ~500–650 °C temperatures that overlap with the GH samples. Samples between 1.2 and 2.2 km above the base of the Chekha Formation vary between ~450–550 °C, and samples from the overlying TH units vary between ~425–550 °C. Thus, comparing the lowest GH samples to the TH samples above the Chekha Formation shows an overall gradual decrease in temperature. The data do not supply evidence for a steep thermal gradient that could demarcate a significant tectonometamorphic discontinuity within the studied thickness of the transect.

6. SHEAR-SENSE, STRAIN, AND VORTICITY DATA

6.1. Shear-Sense Indicators

Shear-sense indicators were observed at both the outcrop and thin-section scale through the full thickness of the transect (Fig. 5). They include

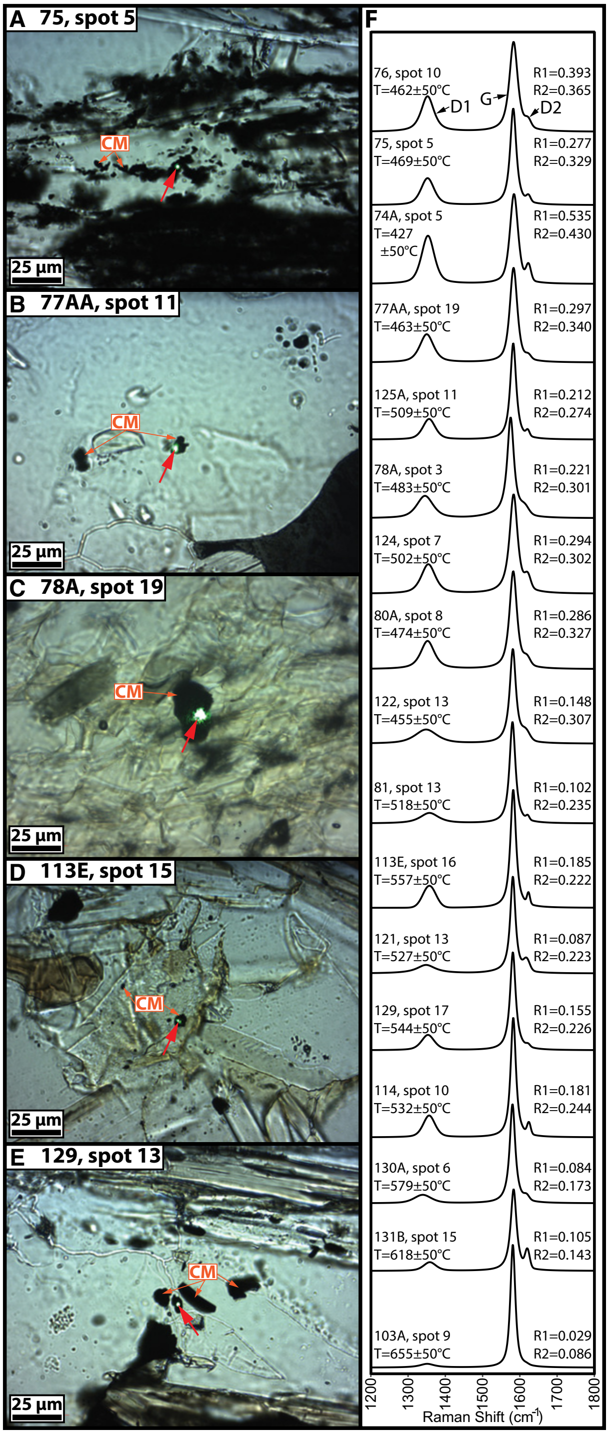

Figure 8. (A–E): Photomicrographs (PPL) of representative examples of analyzed carbonaceous material (CM), which typically occurs as isolated 5–20 µm patches (examples are labeled with orange arrows). The green spot in each photo is the Raman laser beam (labeled with a red arrow). (F) Examples of representative Raman spectra from single-spot analyses of each of the 17 samples, in order of increasing structural height. Positions of the graphite band (G) and defect bands (D1 and D2) are labeled on the top spectrum. Peak temperatures (T) and R1 and R2 parameters are calculated after Rahl et al. (2005). Peak center position, height, amplitude, and area are listed for individual spot analyses in the Data Repository Item. Single spot analyses are listed with errors of ±50 °C, which is the external uncertainty from the Rahl et al. (2005) calibration.

C′-type shear bands (Figs. 10A and 10B), leucosomes, leucogranite bodies, and rigid porphyroclasts sheared into σ-objects (Figs. 10C and 10G), SC fabrics (Figs. 10D and 10E), rotated rigid clasts, asymmetric folds (Fig. 10F), and asymmetric boudinage. Though both senses of shear are observed through nearly the full thickness of the transect, south-vergent shear is dominant below the basal Chekha Formation contact (six versus three shear-sense indicators), and north-vergent shear is dominant above the contact (11 versus six shear-sense indicators). In addition, there were five instances where both senses of shear were observed at the same outcrop or within thin sections from samples collected at the same outcrop (Fig. 5).

6.2. Three-Dimensional Finite Strain of Quartz Porphyroclasts

Most of the examined thin sections exhibit complete recrystallization of quartz (e.g., Fig. 7); however, eight Chekha Formation samples, three Deshichilling Formation samples, and one Maneting Formation sample exhibit non-recrystallized, plastically elongated quartz porphyroclasts that are isolated within a micaceous or calcite-rich matrix (Figs. 11A and 11B; additional photomicrographs in the Data Repository Item). These samples are representative of the different TH lithologies observed on the transect. To quantify the magnitude and orientation of 3D finite strain, the Rf-ϕ method (e.g., Ramsay, 1967; Dunnet, 1969) was performed on quartz porphyroclasts in two foliation-normal thin sections from each sample. One thin section was cut parallel to stretching lineation or normal to crenulation cleavage (thin sections ending with "A"), which is interpreted to approximate the XZ strain plane. The other was cut normal to stretching lineation or parallel to crenulation cleavage (thin sections ending with "B"), which is interpreted to approximate the YZ strain plane (additional methodology details and supporting data in the Data Repository Item). Two-dimensional strain ellipses for individual samples are plotted on Figure 5, and strain data are summarized in Table 3. For all samples, the 2D strain ratio (Rs) in the "A" thin section was either greater than or equivalent within error to Rs in the "B" thin section, and the direction of shortening in all thin sections was sub-normal to foliation.

Competency contrasts between clasts and matrix can result in heterogeneous strain patterns at the thin section and outcrop scale (e.g., Sanderson, 1982; Yonkee, 2005; Holyoke and Tullis, 2006; Yonkee et al., 2013). Experiments and studies of naturally deformed rocks have shown that quartz clasts isolated within a micaceous matrix often exhibit a lower elongation magnitude compared to the matrix (e.g., Tullis and Wenk, 1994; Treagus and Treagus, 2002; Czeck et al., 2009; Yonkee et al., 2013). The data set of Long et al. (2011c) from GH and TH rocks on the Shemgang transect illustrates higher strain magnitudes accommodated by schist and phyllite (median X/Z ratio of 3.0) compared to quartzite (median X/Z value of 1.6), indicating that relative differences in elongation magnitudes between quartz- and mica-rich lithologies are recorded by plastic elongation of quartz clasts. However, because we have no way to quantify the relative elongations of quartz versus mica- or calcite-rich matrix in our samples, we cautiously interpret our strain magnitudes as minima.

Strain ellipsoids from Chekha Formation samples yielded X/Z and Y/Z Rs ratios that range between 2.0–3.5 and 1.6–3.1, respectively (Fig. 5). The highest Rs ratios (X/Z: 2.8–3.5, Y/Z: 2.6–3.1) are observed in the basal ~800 m of the Chekha Formation. The Deshichilling and Maneting Formation samples yielded X/Z and Y/Z ratios that range between 2.5–2.9 and 1.6–2.7, respectively. On a Flinn diagram, all ellipsoids from the Chekha and Deshichilling Formations plot in the apparent flattening field, and the Maneting Formation ellipsoid plots along the plane strain line (Fig. 11C). Phi angles were measured relative to foliation and are therefore equivalent to the parameter θ′, defined as the acute angle between the grain long axis and foliation (e.g., Ramsay and Huber, 1983) (for

TABLE 2. AVERAGE PRESSURE-TEMPERATURE ESTIMATES OF DANG CHU SAMPLES BY THERMOCALC

Sample number	Unit	Rock type	Garnet-biotite thermometry* (°C)	Garnet position	Fluid (X_{H_2O})	Temperature (°C)	1σ	Pressure (kbar)	1σ	Corr.	σ_{fit}	n
BU13-103A	GHIml	Mica-rich quartzite	646	Rim								
BU13-104C	GHIml	Metapelite	634	Core	1	855	53	8.8	1.5	0.816	0.39	7
					0.5	689	38	7.4	1.2	0.803	0.49	7
					0.3	648	35	7.0	1.2	0.809	0.60	7
					0.25	633	34	6.9	1.2	0.81	0.65	7
					0.2	614	33	6.7	1.1	0.811	0.72	7
BU13-126A	Deshichilling	Siliceous gneiss	566	Near rim								
BU13-130B	Chekha	Metapelite	625	Near rim	1	780	44	7.6	1.4	0.839	1.04	5
					0.4	697	36	6.9	1.2	0.85	0.81	5
					0.2	633	32	6.3	1.1	0.856	0.67	5
					0.1	569	28	5.8	1.1	0.86	0.64	5
BU13-131B	Chekha	Metapelite	647	Near rim	1	882	62	9.3	1.6	0.815	1.07	5
					0.5	805	49	8.6	1.4	0.817	0.85	5
					0.2	707	40	7.7	1.3	0.82	0.62	5
					0.12	653	36	7.2	1.2	0.82	0.55	5
					0.1	634	35	7.0	1.2	0.82	0.54	5

Notes: Gray highlighted cells indicate the preferred pressure estimates, determined by changing the X_{H_2O} until the temperature calculated by THERMOCALC matched with the garnet-biotite temperature (e.g., Searle et al., 2003). Corr.—correlation.
*Temperatures calculated at 7 kbar with the 5AV garnet-biotite thermometry calibration of Holdaway (2000).

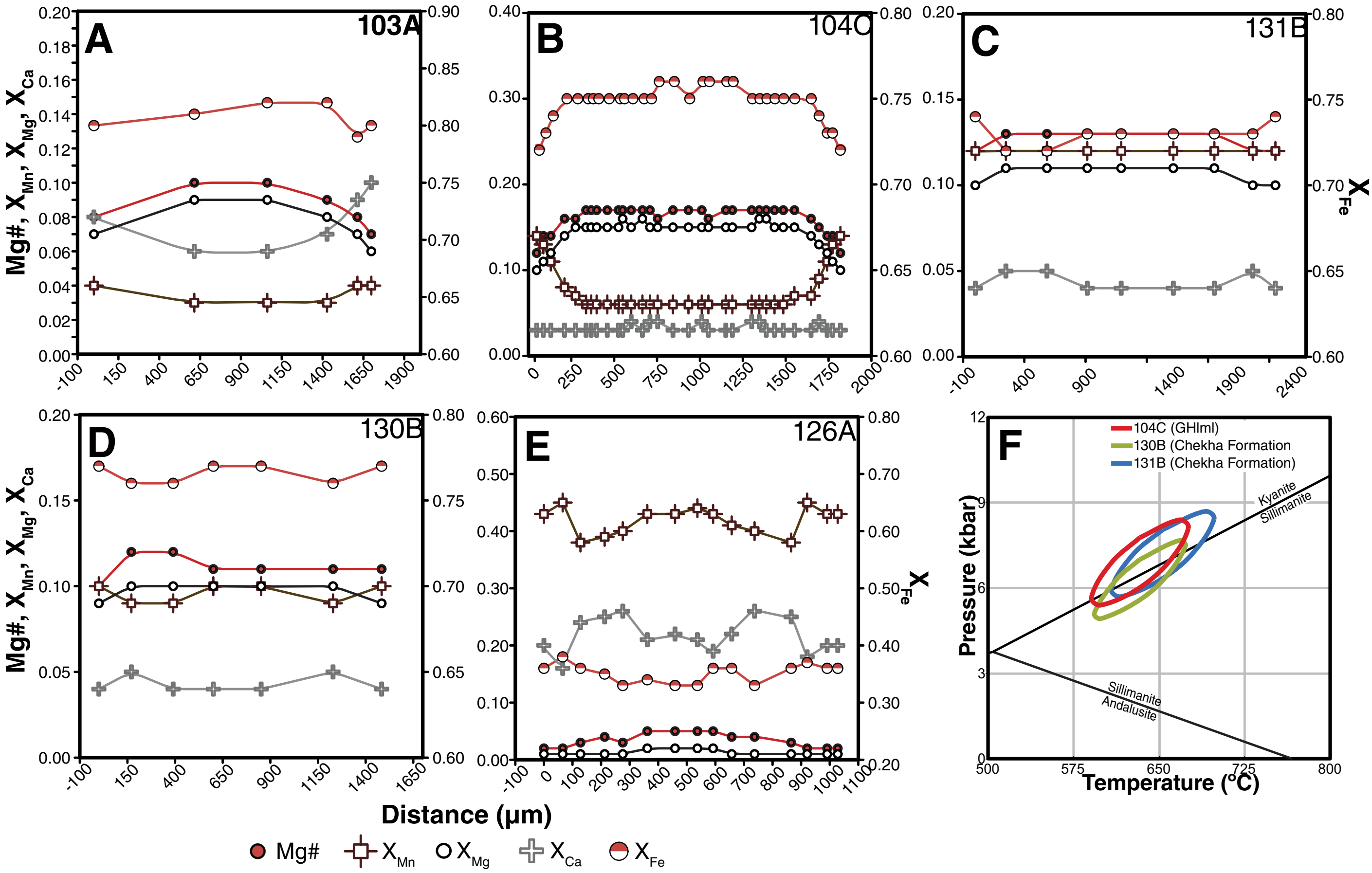

Figure 9. (A–E) Quantitative element profiles of representative garnet from samples 103A, 104C, 131B, 130B, and 126A. The left axis represents the molar proportion of Mg# (Mg/(Mg + Fe)) and three garnet endmembers: spessartine (X_{Mn}), pyrope (X_Mg), and grossular (X_{Ca}). The right axis represents the molar proportion of garnet endmember almandine (X_{Fe}). The horizontal axis is the distance across the rim-to-rim transect. (F) Pressure-temperature results calculated from THERMOCALC for samples 104C, 130B, and 131B.

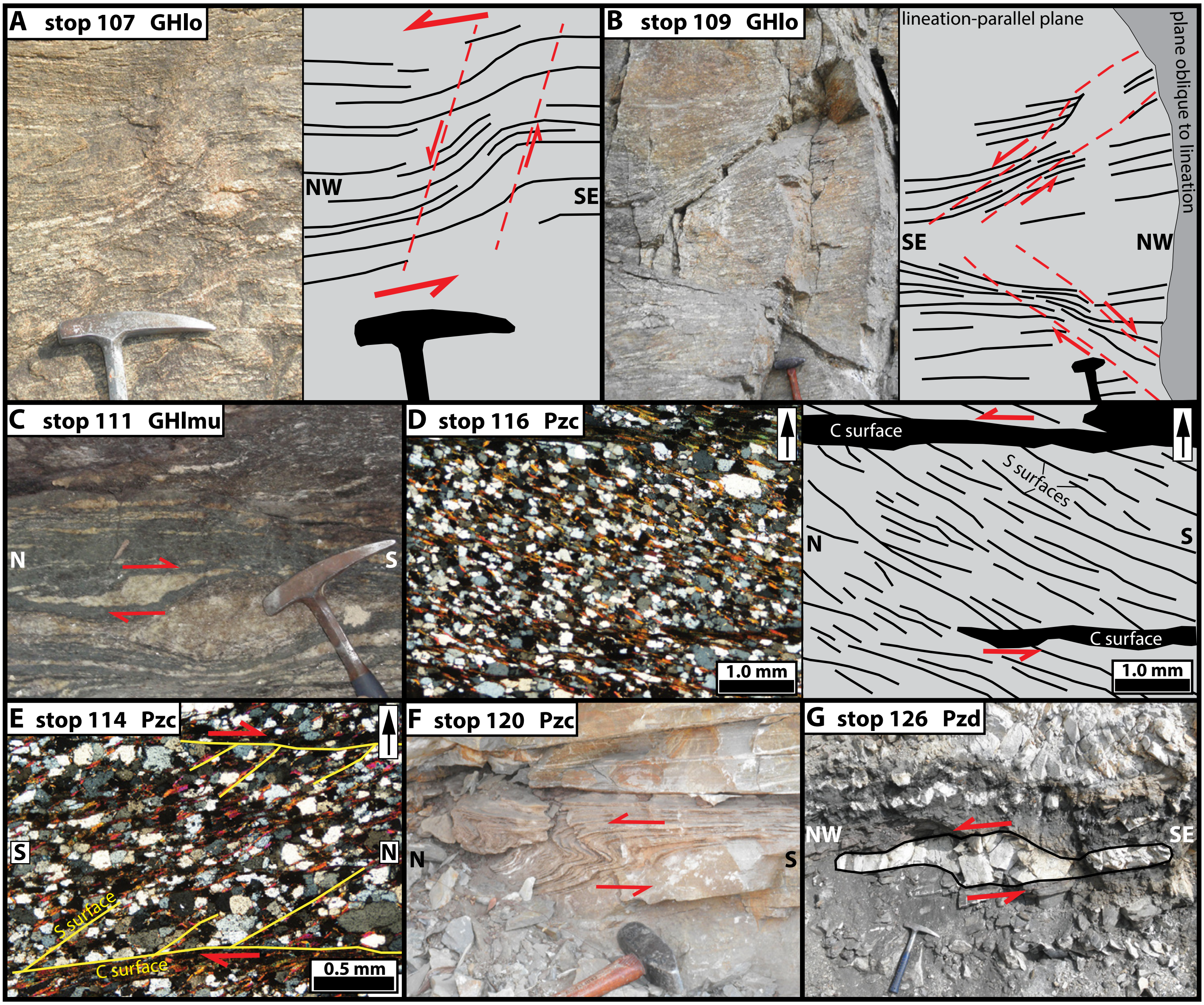

Figure 10. Photographs and photomicrographs illustrating representative shear-sense indicators observed on the Dang Chu transect. (A) Top-down-to-northwest C′-type shear band within GHIo orthogneiss (–3050 m); defines overall top-to-northwest shear sense. (B) Conjugate C′-type shear bands within the same outcrop of GHIo orthogneiss (–2150 m). Upper shear band is top-down-to-southeast, and lower shear band is top-down-to-northwest. (C) Leucosome sheared into top-to-south σ-object within GHImu paragneiss (–1100 m). (D) Top-to-north SC fabric within Chekha Formation micaceous quartzite (+160 m) (XPL; lineation-parallel thin section; arrow points structurally upward). (E) Top-to-north SC fabric within Chekha Formation phyllite (+720 m) (XPL; lineation-parallel thin section; arrow points structurally upward). (F) Top-to-north asymmetric fold in Chekha Formation marble (+1450 m). (G) Foliation-parallel leucogranite body sheared into a top-to-northwest σ-object, within Deshichilling Formation quartzite (+4700 m).

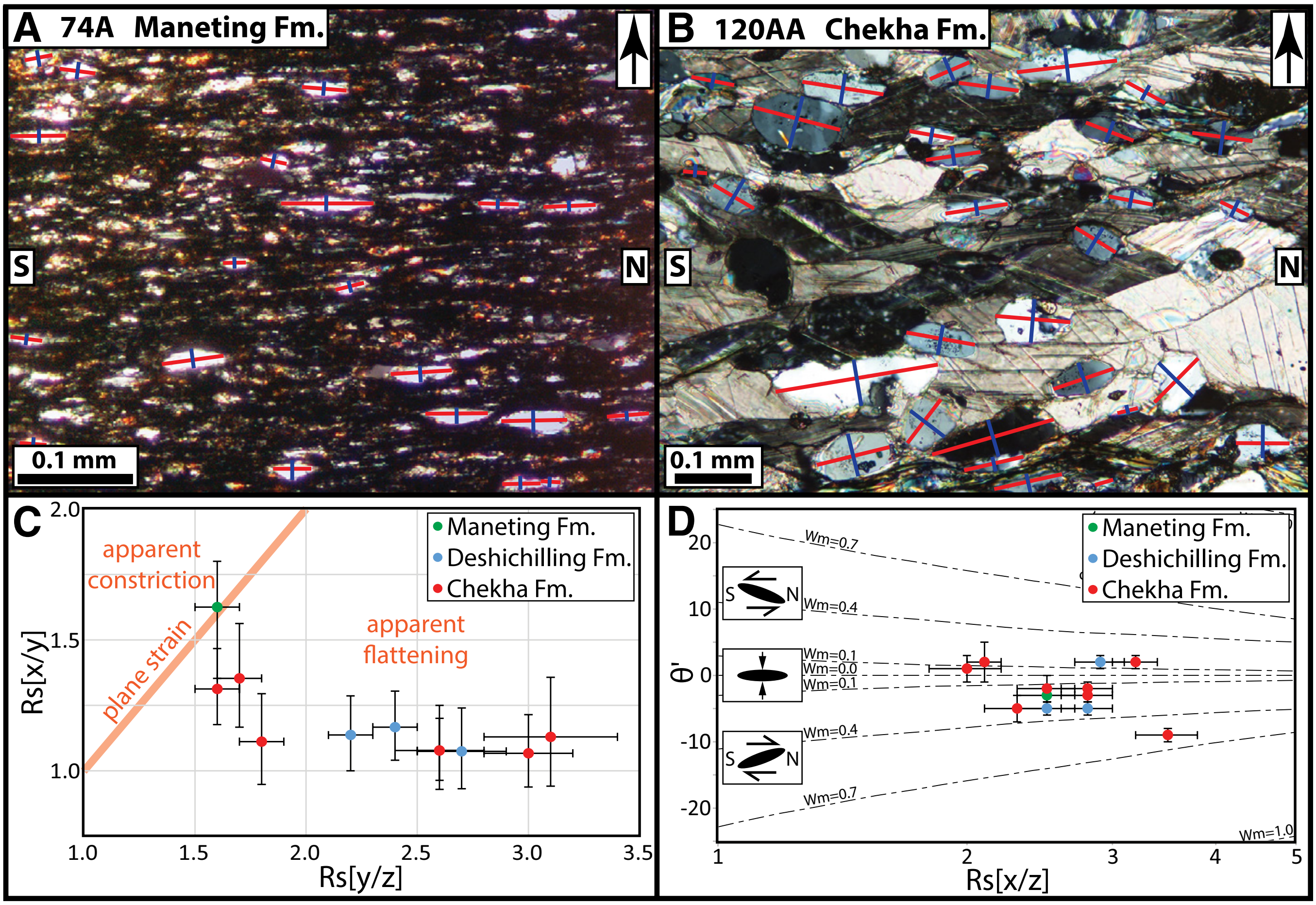

Figure 11. (A and B) Annotated photomicrographs showing representative examples of quartz grain measurements for Rf-ϕ analyses. Photos were taken in XPL, with foliation oriented horizontal; arrow points structurally upward. Photos show scenarios of plastically deformed quartz porphyroclasts isolated within micaceous (A) and calcite-rich matrix (B). Long axes of measured quartz grains shown in red, and short axes shown in blue. (C) Flinn diagram (e.g., Flinn, 1962) showing 3D strain fields for constant-volume deformation. Error bars shown at 1 standard error. (D) Plot of tectonic elongation in lineation-parallel thin sections ($Rs_{[x/z]}$) versus θ′ (e.g., Tikoff and Fossen, 1995), with contours of mean kinematic vorticity for plane strain deformation (W_m) plotted (modified from Yonkee, 2005). Error bars are shown at 1 standard error level.

simplicity, from this point on, ϕ is referred to as θ′). The sign convention used for θ′ is positive if the grain long axis is inclined to the north or east relative to foliation, and negative if inclined to the south or west relative to foliation. In both "A" and "B" thin sections, mean θ′ values are quite low, with 20 of the 23 analyzed thin sections yielding values between ±5°; the remaining samples yielded outlying values of +8°, –9°, and –11°. The similar elongation magnitudes of the X and Y axes, combined with the low θ′ values, indicate that all samples but one (74) experienced layer-normal flattening strain (e.g., Long et al., 2011c).

6.3. Estimation of Mean Kinematic Vorticity Number

The mean kinematic vorticity number (W_m) is a ratio that quantifies the relative contributions of pure shear and simple shear in rocks (e.g., Means et al., 1980; Passchier, 1987; Tikoff and Fossen, 1993; Means, 1994). A W_m value of 0 represents idealized pure shear, a value of 1 represents idealized simple shear, and equal contributions occur at $W_m = 0.71$ (e.g., Law et al., 2004). We estimated W_m within the thin sections cut parallel to lineation (the "A" thin sections) by comparing our data to W_m contours plotted on a graph of Rs versus θ′ (referred to here as the Rs-θ′ method) (Fig. 11D) (e.g., Tikoff and Fossen, 1995). This method assumes that quartz clast ellipticity is the result of approximately homogeneous crystal-plastic elongation in the direction of maximum finite stretching, which is supported by low standard errors for θ′ (typically ±1°–2°) and Rs (typically ±0.1–0.2) values for each analysis. For estimation of W_m, the simplified case of steady-state plane strain is assumed (e.g., Fossen and Tikoff, 1993; Johnson et al., 2009), and since nearly all of the rocks that we analyzed experienced flattening strain, the resulting W_m values are interpreted to represent maxima (Tikoff and Fossen, 1995). Given the relatively low strain magnitudes of our samples (Rs ~1.5–3.5), the overestimation of W_m introduced by assuming plane strain likely does not exceed ~0.05 (Tikoff and Fossen, 1995). The range of W_m values reported for each sample is estimated from the ±1 standard error reported for the mean θ′ value of each sample (Fig. 11D). All W_m ranges are rounded to the nearest 0.05, and corresponding contributions of pure and simple shear (from Law et al., 2004) are rounded to the nearest 5% (Table 3).

Our strain samples yielded W_m values typically between 0.00 and 0.35 (75%–100% pure shear); one sample (129) yielded a W_m range of

TABLE 3. SUMMARY OF FINITE STRAIN AND KINEMATIC VORTICITY DATA FROM THE DANG CHU TRANSECT

Thin section	Map unit	Lithology	Structural height above base Pzc (m)	Foliation (d, dd)	Lineation (tr, pl)	Crenulation axis (tr, pl)	Orientation relative to feature	Thin section orientation (d, dd)	Rs (±1 SE)[1]	φ (equal to θ') (±1 SE)	W_m range from Rs vs. θ' method[2]	Pure shear from Rs vs. θ' method[3] (%)	Quartz porphyroclast type[4]
74A	Maneting	Phyllite	4930	28, 090	-	14, 154	Normal to crenulation	75, 332	2.5 ± 0.2	–3 ± 1°	0.15–0.25	80–90	1
74B							Parallel to crenulation	65, 237	1.6 ± 0.1	8 ± 4°			
125AA	Deshichilling	Phyllite	3980	16, 094	-	16, 100	Normal to crenulation	74, 280	2.9 ± 0.2	2 ± 1°	0.10–0.25	80–95	1
125AB							Parallel to crenulation	89, 188	2.7 ± 0.2	–2 ± 1°			
124A	Deshichilling	Phyllite	3000	19, 000	-	5, 085	Normal to crenulation	88, 267	2.8 ± 0.2	–5 ± 1°	0.25–0.35	75–80	1
124B							Parallel to crenulation	71, 174	2.4 ± 0.1	2 ± 1°			
123BA	Deshichilling	Phyllite	2420	82, 325	25, 052	-	Parallel to lineation	19, 343	2.5 ± 0.2	–5 ± 1°	0.25–0.35	75–80	1
123BB							Normal to lineation	65, 231	2.2 ± 0.1	-5 ± 2°			
120AA	Chekha	Quartzite	1630	10, 340	11, 352	-	Parallel to lineation	87, 081	2.1 ± 0.1	2 ± 3°	0.00–0.30	80–100	2
120AB							Normal to lineation	80, 170	1.6 ± 0.1	–11 ± 3°			
113AA	Chekha	Phyllite	1270	44, 310	4, 226	44, 315	Parallel to lineation	46, 139	2.8 ± 0.2	– ± 1°	0.15–0.25	80–90	1
113AB							Normal to lineation	83, 046	2.6 ± 0.2	–3 ± 1°			
118BA	Chekha	Quartzite	1240	12, 044	06, 338	-	Parallel to lineation	79, 250	2.0 ± 0.2	1 ± 2°	0.00–0.20	85–100	2
118BB							Normal to lineation	85, 159	1.8 ± 0.1	5 ± 2°			
121A	Chekha	Marble	1210	Horizontal	-	-	North-South	90, 270	2.3 ± 0.2	–5 ± 2°	0.20–0.40	70–85	2
121B							East-West	90, 000	1.7 ± 0.1	–4 ± 4°			
128A	Chekha	Phyllite	910	26, 350	27, 000	-	Parallel to lineation	86, 090	2.5 ± 0.2	–2 ± 2°	0.00–0.25	80–100	1
129A	Chekha	Phyllite	790	21, 060	2, 142	-	Parallel to lineation	69, 230	3.5 ± 0.3	–9 ± 1°	0.50–0.65	55–65	1
129B							Normal to lineation	85, 321	3.1 ± 0.3	–4 ± 1°			
114A	Chekha	Phyllite	720	29, 270	0, 000	41, 270	Parallel to lineation	61, 090	3.2 ± 0.2	2 ± 1°	0.10–0.25	80–95	1
114B							Normal to lineation	90, 000	3.0 ± 0.2	–2 ± 1°			
131BA	Chekha	Schist	70	10, 045	4, 348	-	Parallel to lineation	82, 269	2.8 ± 0.2	–2 ± 1°	0.10–0.20	85–95	1
131BB							Normal to lineation	84, 170	2.6 ± 0.1	1 ± 2°			

Notes: Abbreviations: d, dd—dip, dip direction notation; tr, pl—trend, plunge notation. Definitions: Rs—tectonic elongation (long axis to short axis ratio); φ—angle between long axis and foliation (equal to θ' of Ramsay and Huber, 1983). (Sign convention for φ: clockwise from foliation is positive; counterclockwise from foliation is negative). W_m—mean kinematic vorticity number.

[1]Rs values and associated errors are rounded to nearest 0.1. After discussions in the text, Rs values are interpreted to likely represent minima for bulk-rock strain.

[2]Estimated W_m values are rounded to nearest 0.05.

[3]Percent pure shear values were determined from Law et al. (2004) and are rounded to nearest 5%.

[4]Type 1—quartz porphyroclasts isolated within micaceous matrix; Type 2—quartz porphyroclasts isolated within calcite matrix.

0.50–0.65 (55%–65% pure shear). The low W_m values obtained on the Dang Chu transect are similar to those obtained above and below the MCT in eastern and central Bhutan (Long et al., 2011c, 2016).

7. COMPILATION OF TEMPERATURE, PRESSURE, STRAIN, AND SHEAR-SENSE DATA FROM CENTRAL BHUTAN

In order to define robust trends with structural distance, we integrate the T, P, strain, and shear-sense data from the Dang Chu transect with published data from the Shemgang transect in central Bhutan (Long et al., 2011c; Corrie et al. 2012) and the Sarpang transect in south-central Bhutan (Long et al., 2016) (see Fig. 2 for transect locations). The data are plotted on Figure 12 versus structural height relative to the MCT (see Data Repository Item for data tables and details on structural height estimation).

Temperature data have been estimated from above and below the MCT (Fig. 12A). Below the Shumar thrust, ~3–5 km below the MCT, temperatures are ~300–400 °C. Above the Shumar thrust, between 2.3 and 1.0 km below the MCT, temperatures overlap between ~400–550 °C. Between 1 and 0 km below the MCT, temperatures increase from ~400–500 °C to ~600–750 °C, defining a steep, inverted field gradient (Long et al., 2016). Above the MCT, peak temperatures become gradually cooler with structural distance, from ~600–750 °C at the MCT, to ~400–500 °C at a height of 11 km. Contoured isotherms are subparallel to the MCT (Fig. 12E) and are not telescoped in proximity to the different mapped structural positions of the STD.

Pressure data are only available from rocks at and above the MCT (Fig. 12B). Pressures gradually decrease with structural distance, from ~9.5–11.5 kbar at the MCT to ~4.0–6.5 kbar at a height of 10 km. The difference in pressures between the top and bottom of this interval defines a field gradient that is ~1.2–2.4 times greater than a typical lithostatic gradient of 0.27 kbar/km, suggesting postmetamorphic flattening of rocks above the MCT (e.g., Corrie et al., 2012).

Finite strain data from the Dang Chu (this study), Shemgang (Long et al., 2011c), and Sarpang transects (Long et al., 2016) were compiled for samples above and below the MCT. Using methods outlined in Law (2010) and Xypolias et al. (2010), strain magnitude and kinematic vorticity were incorporated to calculate transport-parallel lengthening and transport-normal shortening for individual strain analyses (see Data Repository Item for additional information) (Figs. 12C and 12D). Because the lengthening and shortening values are calculated from minimum strain estimates (see section 6.2 above), we similarly interpret them as minima. Below the Shumar Thrust, lengthening is between ~0%–20% (with one outlier at ~42%), and shortening is between ~7%–25%. Between the ST and the MCT, lengthening is between ~40%–80% and shortening is between ~35%–50%. Due to complete recrystallization of quartz, no finite strain data are available between 0 and 2 km above the MCT. Above this level, the data exhibit significant variability, which is attributed to multiple lithologies being analyzed (e.g., Long et al., 2011c, their fig. 13C), but can be divided by strain magnitude into two general domains. Between 2 and 5 km above the MCT, transport-parallel lengthening varies between ~0%–180%, and transport-normal shortening between ~12%–65%. Average values (with 1σ error) are 66 ± 45% for lengthening and 40 ± 13% for shortening. Between 5 and 11 km above the MCT, lengthening varies between ~0%–67% (with one outlier at ~115%), and shortening between ~0%–50%. Average values are 30 ± 24% for lengthening and 30 ± 12% for shortening (1σ).

A compilation of shear-sense indicators observed in outcrops, thin sections, and quartz *c*-axis pole plots in central Bhutan (n = 84; Long and McQuarrie, 2010; Long et al., 2016; this study; see Data Repository Item for additional details) is plotted in a histogram showing the total number of top-to-south and top-to-north shear-sense indicators observed versus structural height (Fig. 12F). Both senses of shear are observed through the full structural thickness of analyzed rocks. However, top-to-north shear-sense indicators are prevalent between 2 and 11 km above the MCT and are dominant above a height of 6 km.

8. DISCUSSION

8.1. Arguments Against the Presence of a Discrete, Normal-Sense Shear Zone in Central Bhutan

We argue that the compiled metamorphic, strain, and shear-sense data rule out the presence of a discrete, normal-sense shear zone above the MCT in central Bhutan. There are no observed transitions from undeformed or weakly deformed rocks to strongly deformed rocks, as would be expected for the boundaries of a shear zone (e.g., Simpson and DePaor, 1993). Instead, we have demonstrated that the rocks have been penetratively deformed and completely (or nearly completely) recrystallized at all structural levels. Previous studies have interpreted the presence of shear-sense indicators such as SC fabrics and shear bands to delineate zones of locally intense north-vergent shear that they interpret as the STD (Grujic et al., 2002; Kellett et al., 2009; Greenwood et al., 2016). However, our compilation demonstrates that these and other top-to-north shear-sense indicators are not spatially concentrated, but instead are broadly distributed through GH and TH rocks (Fig. 12F).

Interpreting trends in temperature and pressure to assess the presence or absence of a structure requires that the timing of metamorphism was approximately coeval in the studied rocks (e.g., England and Thompson, 1984). Though data estimating the timing of metamorphism on the Dang Chu and Shemgang transects are not available, geochronologic data collected in other regions of Bhutan illustrate that metamorphism of GH and TH rocks below the Kakthang and Laya thrusts was broadly coeval. The youngest ages of prograde monazite growth and zircon rim growth, which have been interpreted to indicate the timing of near-peak to peak metamorphism, are typically between ca. 23–20 Ma (Daniel et al., 2003; Kellett et al., 2010; Chambers et al., 2011; Tobgay et al., 2012; Zeiger et al., 2015).

Others have proposed that a normal-sense shear zone such as the STD would not be predicted to exhibit a clear metamorphic discontinuity if it accommodated motion subparallel to isotherms (Godin et al., 2011). This scenario would leave open the possibility that a discrete, normal-sense shear zone could still be present in central Bhutan. However, this is not supported by the broad vertical distribution of ductile fabrics and recrystallization and the vertical patterns of finite strain and shear-sense indicators that we document (Figs. 12C, 12D, and 12F). In addition, thermal models based on Himalayan parameters show that isotherms produced through protracted continental underthrusting are not flat but instead are sigmoidally folded across strike, at a scale of tens of km (Royden, 1993; Henry et al., 1997; Bollinger et al., 2006; Herman et al., 2010). This thermal regime produces both vertical (temperatures increase downward) and lateral (temperatures increase northward) geothermal gradients in much of the orogen (e.g., Corrie and Kohn, 2011, their fig. 7). Thus, even if a shear zone were subparallel to isotherms in some areas (i.e., toward the foreland), it would not be in portions that are farther toward the hinterland. Therefore, long-distance (≥~100 km) lateral transport along a discrete (≤~1-km-thick), normal-sense shear zone through such a thermal regime would be predicted to yield a compressed, upright thermal field gradient (e.g., Kohn, 2008, 2014; Corrie and Kohn, 2011).

Quantitative studies of the metamorphic conditions across the STD in other parts of the Himalaya (Cottle et al., 2011; Law et al., 2011), including the Lingshi region in northwest Bhutan (Kellett and Grujic, 2012),

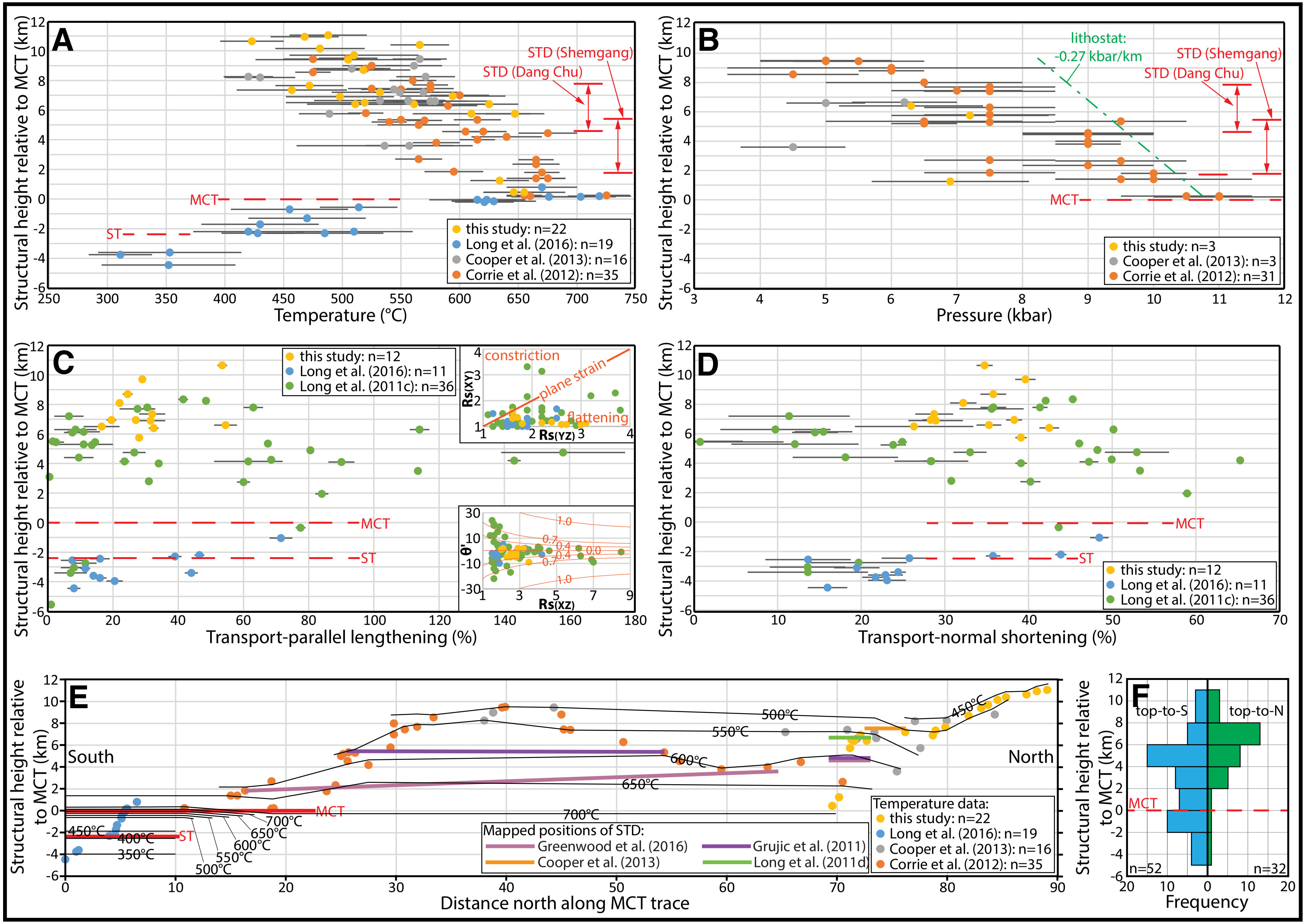

Figure 12. Compiled temperature, pressure, shear-sense, and strain data from central Bhutan, plotted against structural height relative to the Main Central thrust (MCT) (see Data Repository Item for data tables and details on structural height estimation). ST—Shumar thrust. (A) Temperature versus structural distance; the range of mapped structural positions of the South Tibetan detachment (STD) on the Shemgang and Dang Chu transects are shown (from Grujic et al., 2011; Long et al., 2011d; Cooper et al., 2013; and Greenwood et al., 2016; also see Fig. 2). (B) Pressure versus structural distance; lithostatic gradient shown for reference. (C) Transport-parallel lengthening versus structural distance. The upper inset is a Flinn diagram (e.g., Flinn, 1962), showing that the majority of analyses fall within the flattening field. The lower inset is a plot of θ′ versus $Rs_{(X/Z)}$, with lines of equal W_m value contoured (modified from Tikoff and Fossen, 1995). (D) Transport-normal shortening versus structural distance. (E) Distance north of the southernmost sample (sample 1A of Long et al., 2016), as measured along the trace of the MCT on the Mangde Chu cross section of Long et al. (2011b) (Dang Chu and Sarpang transect samples were projected east to their respective positions on the Mangde Chu cross section). Peak temperature data are contoured at a 50 °C interval. (F) Frequency histogram of shear-sense indicators observed versus structural distance.

have documented upright thermal field gradients of ~300–400 °C/km distributed through shear zones as thin as ~0.5–1.0 km. This extreme telescoping of isotherms contrasts markedly with our data from central Bhutan, where we document a continuous, gradual decrease in T and P between 0 and 11 km above the MCT. Therefore, we argue that there is no obvious, discrete shear zone in central Bhutan that can be recognized by a marked change in P or T conditions. We acknowledge that we cannot rule out the existence of second-order shear zones that exhibit a metamorphic discontinuity below the threshold of the data errors, and that alternative interpretations that permit the existence of a discrete shear zone are possible (e.g., Godin et al., 2011); however, as discussed above, our analyses of fabrics, finite strain, and shear sense did not yield evidence for any discrete shear zones.

The distributed, super-lithostatic pressure gradient above the MCT in central Bhutan was originally documented by Corrie et al. (2012) and is supported here with additional data (Fig. 12B). Using a series of different geometric scenarios, Corrie et al. (2012) argued that this pressure gradient could not have been generated through instantaneous overthrusting, by pre- or syn-metamorphic continuous thrusting, or through post-metamorphic simple shear within an inclined slab. Thus, we follow the interpretation of Corrie et al. (2012) that the super-lithostatic gradient is a consequence of post-peak metamorphic flattening, accommodated by distributed north-vergent shearing.

Our data sets inspire a return to the pioneering work of Gansser (1983), who interpreted the contact between GH and TH rocks in central Bhutan as conformable and metamorphically gradational. Some studies have interpreted the lower-grade metamorphic assemblages and evidence for deformation at lower apparent temperatures with increasing structural level as supporting evidence for the STD (Grujic et al., 2002; Kellett et al., 2009; Cooper et al., 2013; Greenwood et al., 2016); however, we argue that these features can instead be viewed as predictable consequences of a distributed, upright metamorphic field gradient. These changes are commensurate with the thickness of rocks involved, in particular when the super-lithostatic gradient is restored. The present 11 km thickness restores to a pre-flattening thickness of 20 ± 7 km, and based on pressures at the base and top, the exposed interval spanned approximate peak depths between ~40 and ~20 km.

8.2. Kinematic Implications of Distributed North-Vergent Shearing in Central Bhutan

The strain data highlight greater average transport-parallel lengthening at 2–5 km above the MCT than at 5–11 km above the MCT (Figs. 12C and 12D). This imparts an overall top-to-north shear strain within this interval (Fig. 13), which is corroborated by north-vergent shear-sense indicators distributed between 2 and 11 km above the MCT (Fig. 12F). An ~80 km north-south length of GH rocks in the hanging wall of the MCT can be measured between the traces of the MCT and the Kakthang thrust on a cross section through the Shemgang transect (Long et al., 2011b). Using this length, and the average (±1σ) transport-parallel lengthening values listed above, this corresponds to approximate minimum ranges of ~17–89 km of lengthening between 2 and 5 above the MCT, and ~5–43 km of lengthening between 5 and 11 km above the MCT. Therefore, these data allow for as much as ~85 km of minimum north-vergent shearing to be distributed above the MCT in central Bhutan. This distributed shearing may be the result of a vertical gradient in southward transport magnitudes that developed during motion on the MCT, or alternatively may be related to motion on the STD system mapped to the north. We explore these alternative interpretations below.

Long et al. (2016) documented an upward increase in transport-parallel lengthening beneath the MCT on the Sarpang transect (Fig. 12C), and they estimated ~40–50 km of differential southward transport between 2.3 and 1.0 km below the MCT. Therefore, taken together with the observations in the hanging wall, transport-parallel lengthening increases as the MCT is approached from above and below (Fig. 13). These lengthening gradients imply that penetrative fabrics, shearing, and internal strain observed through the studied thickness of rocks are genetically related to motion on the MCT, which acted as a stretching fault (Long et al., 2016). Therefore, the distributed north-vergent shearing could have developed as a result of differential southward transport magnitudes during motion on the MCT,

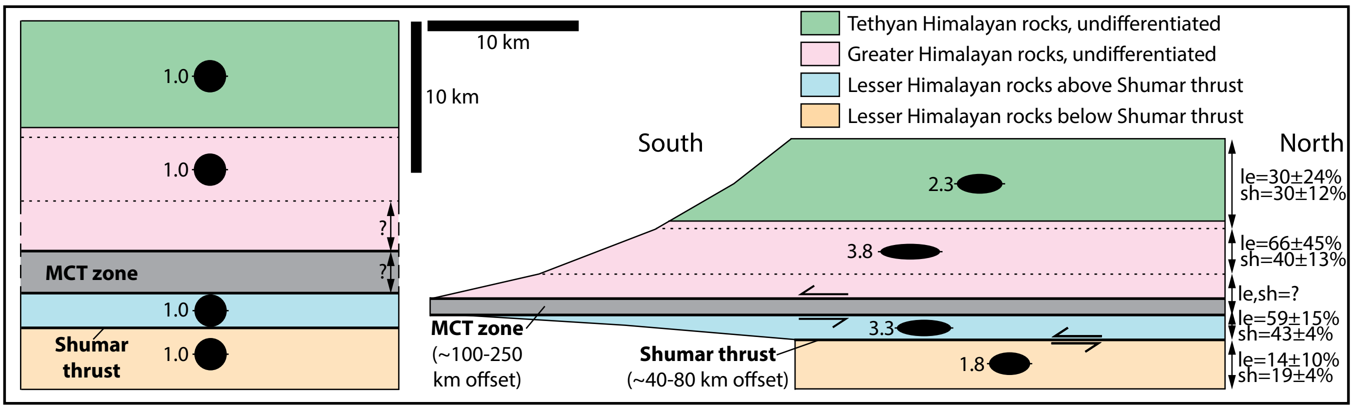

Figure 13. Diagrams illustrating the approximate minimum change in transport-parallel dimensions of a 25-km-long section of Greater Himalayan (GH) and Tethyan Himalayan (TH) rocks above the Main Central thrust (MCT) and Lesser Himalayan (LH) rocks below, before and after the measured finite strain. The diagram on the left shows original length and thicknesses. Restored thicknesses of the MCT zone and GH rocks just above the MCT zone are queried, because strain could not be quantified through this interval. The diagram on the right shows final observed thicknesses, approximate deformed lengths, strain ellipses showing average X/Z elongations, and average lengthening (le) and shortening (sh) values (with 1σ error) for each finite strain domain (note: after discussions in the text, strain, lengthening, and shortening magnitudes likely represent minima). Offset magnitudes for the MCT and Shumar thrust are from Long et al. (2016). The MCT zone is delineated from the upper and lower limits of inverted metamorphism reported in Long et al. (2016).

as expressed by the gradient in transport-parallel lengthening as the MCT is approached from above (Fig. 13).

Alternatively, the distributed north-vergent displacement above the MCT may be genetically related to offset accommodated along the STD system mapped to the north. The distributed displacement may have been fed northward into a more discrete shear zone, similar to the STD documented in the Lingshi region (e.g., Kellett and Grujic, 2012). Field relationships that would allow evaluation of this are obscured, because GH rocks in central Bhutan are bound on the north by the out-of-sequence (ca. 15–11 Ma) Kakthang and Laya thrusts (e.g., Grujic et al., 2002; Kellett et al., 2009; Warren et al., 2011). Our strain data allow for ~85 km of minimum north-vergent shear displacement in central Bhutan, which is compatible with the ~65 km minimum offset estimated for the STD at Lingshi (Cooper et al., 2012). Also, the ~5 kbar pressures obtained from TH rocks at the top of the examined section in central Bhutan (Corrie et al., 2012) indicate that ~20 km of rock have been eroded off the top of this section. Therefore, it is also possible that the thick interval of distributed shear in central Bhutan was capped by a discrete, north-vergent shear zone that has since been eroded.

Several studies have proposed that motion on the STD and MCT in Bhutan was coeval and is bracketed between ca. 23 and ca. 15 Ma (Grujic et al., 2002; Daniel et al., 2003; Kellett et al. 2009, 2010; Chambers et al., 2011; Tobgay et al., 2012). Timing estimates for north-vergent shearing in central Bhutan are available from the Ura region, where Kellett et al. (2009, 2010) interpreted that shearing can be bracketed between ca. 22–20 Ma, the timing of youngest ages of prograde monazite growth in GH rocks, and ca. 15.5 Ma. the timing of youngest zircon rim growth in a late-stage, synkinematic leucogranite. Therefore, either scenario (distributed north-vergent shearing resulting from differential southward transport during MCT motion or being translated northward to the STD) is compatible with existing timing estimates, and both are permissible because the STD and MCT have been interpreted to be coeval (e.g., Grujic et al., 2002; Kellett et al., 2009, 2010). Regardless of the specific scenario, the distributed shear and flattening documented in central Bhutan contrasts with the heterogeneous structural thinning typically observed across the STD system (e.g., Searle and Rex, 1989; Searle et al., 2002; Cottle et al., 2011; Law et al., 2011; Kellett and Grujic, 2012). This highlights the broad geometric range of processes that accommodate structural thinning during orogenesis.

9. CONCLUSIONS

1. Temperatures from the Dang Chu transect define a gradual, structurally upward decrease from ~600–700 °C to ~400–500 °C. Compilation of temperature and pressure data from central Bhutan defines a trend of gradual, structurally upward cooling from ~600–750 °C to ~400–500 °C and a structurally upward decrease from 9.5–11.5 kbar to 4.0–6.5 kbar, between 0 and 11 km above the MCT. The pressure data define a distributed field gradient that is ~1.2–2.4 times lithostatic, and restoration of this gradient indicates that 9 ± 7 km of post-peak metamorphic, distributed structural thinning was accommodated above the MCT. These distributed pressure and temperature gradients do not support the existence of a discrete, normal-sense shear zone.

2. Finite strain analyses illustrate that pure shear-dominant ($W_m \leq 0.4$), layer-normal flattening strain was broadly distributed above the MCT. Minimum transport-parallel lengthening ranges between ~20%–110% at 2–5 km above the MCT and between ~5%–55% at 5–11 km above the MCT; this imparted an overall top-to-north shear strain, which is corroborated by distributed north-vergent shear-sense indicators. The strain data allow for ~85 km of minimum north-vergent displacement distributed through these rocks.

3. Distributed north-vergent shearing may be related to a vertical gradient in southward displacement magnitude that developed during motion on the MCT, as expressed by the increase in transport-parallel lengthening as the MCT is approached from above. Alternatively, distributed north-vergent shearing may be related to motion on the STD system to the north, with this displacement translated northward to a discrete shear zone such as that documented in northwest Bhutan (e.g., Kellett and Grujic, 2012). Either scenario is permissible with existing timing estimates on MCT motion, STD motion, and north-vergent shearing in central Bhutan, which are all bracketed between ca. 23–15 Ma.

4. Central Bhutan serves as a case study for large-scale, distributed structural thinning, which contrasts with the style of heterogeneous structural thinning typically observed across the STD system. This highlights the variability in styles of tectonic denudation during orogenesis.

ACKNOWLEDGMENTS

We would like to thank the government of Bhutan, in particular Ugyen Wangda, Tashi Tenzin, and Yonten Phuntsho of the Department of Geology and Mines in the Ministry of Economic Affairs. We are indebted to Owen Neill at the Washington State University School of the Environment. This paper also benefitted from conversations with Matt Kohn. Thoughtful reviews from K. Larson, an anonymous reviewer, and editor L. Godin greatly improved this paper. This work was funded by National Science Foundation grant EAR-1220300 awarded to S. Long and S. Gordon.

REFERENCES CITED

Agustsson, K.M., Gordon, S.M., Long, S.P., Seward, G.G.E., Zeiger, K., and Penfold, M., 2016, Pressure-temperature-structural distance relationships within Greater Himalayan rocks in eastern Bhutan: Implications for emplacement models: Journal of Metamorphic Geology, v. 34, p. 641–662, doi:10.1111/jmg.12197.

Allmendinger, R.W., Cardozo, N., and Fisher, D., 2011, Structural geology algorithms: Vectors and tensors in structural geology: New York, Cambridge University Press, 304 p, doi:10.1017/CBO9780511920202.

Antolín, B., Godin, L., Wemmer, K., and Nagy, C., 2013, Kinematics of the Dadeldhura klippe shear zones (W Nepal): Implications for the foreland evolution of the Himalayan metamorphic core: Terra Nova, v. 25, p. 282–291, doi:10.1111/ter.12034.

Aoya, M., Kouketsu, Y., Endo, S., Shimizu, H., Mizukami, T., Nakamura, D., and Wallis, S., 2010, Extending the applicability of the Raman carbonaceous-material geothermometer using data from contact metamorphic rocks: Journal of Metamorphic Geology, v. 28, p. 895–914, doi:10.1111/j.1525-1314.2010.00896.x.

Beaumont, C., Jamieson, R.A., Nguyen, M.H., and Lee, B., 2001, Himalayan tectonics explained by extrusion of a low-viscosity crustal channel coupled to focused surface denudation: Nature, v. 414, p. 738–742, doi:10.1038/414738a.

Beyssac, O., Goffe, B., Chopin, C., and Rouzaud, J., 2002, Raman spectra of carbonaceous material in metasediments: A new geothermometer: Journal of Metamorphic Geology, v. 20, p. 859–871, doi:10.1046/j.1525-1314.2002.00408.x.

Beyssac, O., Goffe, B., Petitet, J.P., Froigneux, E., Moreau, M., and Rouzaud, J.N., 2003, On the characterization of disordered and heterogeneous carbonaceous materials by Raman spectroscopy: Spectrochimica Acta Part A, v. 59, p. 2267–2276, doi:10.1016/S1386-1425(03)00070-2.

Bhargava, O.N., 1995, The Bhutan Himalaya: A Geological Account: Geological Survey of India, Special Publication Series, v. 39, 245 p.

Bhattacharyya, K., and Mitra, G., 2009, A new kinematic evolutionary model for the growth of a duplex—An example from the Rangit duplex, Sikkim Himalaya, India: Gondwana Research, v. 16, p. 697–715, doi:10.1016/j.gr.2009.07.006.

Bollinger, L., Henry, P., and Avouac, J-P., 2006, Mountain building in the Nepal Himalaya: Thermal and kinematic model: Earth and Planetary Science Letters, p. 244, p. 58–71.

Bordet, P., Colchen, M., Krummenacher, D., Le Fort, P., Mouterde, R., and Remy, M., 1971, Recherches géologiques dans l'Himalaya du Népal: Région de la Thakkhola: Paris, France, Éditions du Centre National de la Recherche Scientifique, 279 p.

Brown, R.L., and Nazarchuk, J.H., 1993, Annapurna detachment fault in the Greater Himalaya of central Nepal, *in* Treloar, P.J., and Searle, M.P., eds., Himalayan Tectonics: Geological Society of London Special Publication 74, p. 461–473, doi:10.1144/GSL.SP.1993.074.01.31.

Burchfiel, B.C., Chen, Z.L., Hodges, K.V., Liu, Y.P., Royden, L.H., Deng, C.R., and Xu, J.N., 1992, The South Tibetan detachment system, Himalayan orogen: Extension contemporaneous with and parallel to shortening in a collisional mountain belt: Geological Society of America Special Paper 269, 41 p.

Burg, J.P., Brunel, M., Gapais, D., Chen, G.M., and Liu, G.H., 1984, Deformation of leucogranites of the crystalline Main Central thrust sheet in southern Tibet (China): Journal of Structural Geology, v. 6, p. 535–542, doi:10.1016/0191-8141(84)90063-4.

Caby, R., Pêcher, A., and Le Fort, P., 1983, Le grand chevauchement central himalayen: Nouvelles données sur le métamorphisme inverse à la base de la Dalle du Tibet: Revue de Géologie Dynamique et de Géographie Physique, v. 24, p. 89–100.

Chambers, J., Parrish, R., Argles, T., Harris, N., and Horstwood, M., 2011, A short-duration pulse of ductile normal shear on the outer South Tibetan detachment in Bhutan: Alternating channel flow and critical taper mechanics of the eastern Himalaya: Tectonics, v. 30, TC2005, doi:10.1029/2010TC002784.

Colchen, M., Le Fort, P., and Pêcher, A., 1981, Geological map of Annapurnas-Manaslu-Ganesh Himalaya of Nepal, *in* Gupta, H.K., and Delany, F.M., eds., Zagros-Hindu Kush-Himalaya geodynamic evolution: Washington, D.C., American Geophysical Union, scale 1:200,000.

Cooper, F.J., Adams, B.A., Edwards, C.S., and Hodges, K.V., 2012, Large normal-sense displacement on the South Tibetan fault system in the eastern Himalaya: Geology, v. 40, p. 971–974, doi:10.1130/G33318.1.

Cooper, F.J., Hodges, K.V., and Adams, B.A., 2013, Metamorphic constraints on the character and displacement of the South Tibetan fault system, central Bhutanese Himalaya: Lithosphere, v. 5, p. 67–81, doi:10.1130/L221.1.

Corrie, S.L., and Kohn, M.J., 2011, Metamorphic history of the central Himalaya, Annapurna region, Nepal, and implications for tectonic models: Geological Society of America Bulletin, v. 123, p. 1863–1879, doi:10.1130/B30376.1.

Corrie, S.L., Kohn, M.J., McQuarrie, N., and Long, S.P., 2012, Flattening the Bhutan Himalaya: Earth and Planetary Science Letters, v. 349–350, p. 67–74, doi:10.1016/j.epsl.2012.07.001.

Cottle, J.M., Waters, D.J., Riley, D., Beyssac, O., and Jessup, M.J., 2011, Metamorphic history of the south Tibetan detachment system, Mt. Everest region, revealed by RSCM thermometry and phase equilibria modeling: Journal of Metamorphic Geology, v. 29, p. 561–582, doi:10.1111/j.1525-1314.2011.00930.x.

Czeck, D.M., Fissler, D.A., Horsman, E., and Tikoff, B., 2009, Strain analysis and rheology contrasts in polymictic conglomerates: An example from the Seine metaconglomerates, Superior Province, Canada: Journal of Structural Geology, v. 31, p. 1365–1376, doi:10.1016/j.jsg.2009.08.004.

Daniel, C.G., Hollister, L.S., Parrish, R.R., and Grujic, D., 2003, Exhumation of the Main Central Thrust from lower crustal depths, eastern Bhutan Himalaya: Journal of Metamorphic Geology, v. 21, p. 317–334, doi:10.1046/j.1525-1314.2003.00445.x.

Davidson, C., Grujic, D.E., Hollister, L.S., and Schmid, S.M., 1997, Metamorphic reactions related to decompression and synkinematic intrusion of leucogranite, High Himalayan crystallines, Bhutan: Journal of Metamorphic Geology, v. 15, p. 593–612, doi:10.1111/j.1525-1314.1997.tb00638.x.

DeCelles, P.G., Gehrels, G.E., Quade, J., LaReau, B., and Spurlin, M., 2000, Tectonic implications of U-Pb zircon ages of the Himalayan orogenic belt in Nepal: Science, v. 288, p. 497–499, doi:10.1126/science.288.5465.497.

DeCelles, P.G., Robinson, D.M., Quade, J., Ojha, T.P., Garzione, C.N., Copeland, P., and Upreti, B.N., 2001, Stratigraphy, structure, and tectonic evolution of the Himalayan fold-thrust belt in western Nepal: Tectonics, v. 20, p. 487–509, doi:10.1029/2000TC001226.

DeCelles, P.G., Robinson, D.M., and Zandt, G., 2002, Implications of shortening in the Himalayan fold-thrust belt for uplift of the Tibetan Plateau: Tectonics, v. 21, no. 6, 1062, p. 12-1–12-25, doi:10.1029/2001TC001322.

Dunnet, D., 1969, A technique for finite strain analysis using elliptical particles: Tectonophysics, v. 7, p. 117–136, doi:10.1016/0040-1951(69)90002-X.

Edwards, M.A., and Harrison, T.M., 1997, When did the roof collapse?: Late Miocene north-south extension in the high Himalaya revealed by Th-Pb monazite dating of the Khula Kangri granite: Geology, v. 25, p. 543–546, doi:10.1130/0091-7613(1997)025<0543:WDTRCL>2.3.CO;2.

Edwards, M.A., Kidd, W.S.F., Jixiang, L., Yue, Y., and Clark, M., 1996, Multi-stage development of the southern Tibetan detachment system near Khula Kangri: New data from Gonto La: Tectonophysics, v. 260, p. 1–19, doi:10.1016/0040-1951(96)00073-X.

England, P.C., and Thompson, A.B., 1984, Pressure-temperature-time paths of regional metamorphism, Part I: Heat transfer during the evolution of regions of thickened continental crust: Journal of Petrology, v. 25, p. 894–928, doi:10.1093/petrology/25.4.894.

Flinn, D., 1962, On folding during three-dimensional progressive deformation: Quarterly Journal of the Geological Society of London, v. 118, p. 385–428, doi:10.1144/gsjgs.118.1.0385.

Fossen, H., and Tikoff, B., 1993, The deformation matrix for simultaneous simple shearing, pure shearing and volume change, and its application to transpression-transtension tectonics: Journal of Structural Geology, v. 15, p. 413–422, doi:10.1016/0191-8141(93)90137-Y.

Gansser, A., 1964, Geology of the Himalayas: New York, Wiley-Interscience, 289 p.

Gansser, A., 1983, Geology of the Bhutan Himalaya: Basel, Switzerland, Birkäuser, 181 p.

Gehrels, G.E., DeCelles, P.G., Martin, A., Ojha, T.P., and Pinhassi, G., 2003, Initiation of the Himalayan orogen as an early Paleozoic thin-skinned thrust belt: GSA Today, v. 13, p. 4–9, doi:10.1130/1052-5173(2003)13<4:IOTHOA>2.0.CO;2.

Gehrels, G.E., DeCelles, P.G., Ojha, T.P., and Upreti, B.N., 2006a, Geologic and U-Th-Pb geochronologic evidence for early Paleozoic tectonism in the Kathmandu thrust sheet, central Nepal Himalaya: Geological Society of America Bulletin, v. 118, p. 185–198, doi:10.1130/B25753.1.

Gehrels, G.E., DeCelles, P.G., Ojha, T.P., and Upreti, B.N., 2006b, Geologic and U-Pb geochronologic evidence for early Paleozoic tectonism in the Dadeldhura thrust sheet, far-west Nepal Himalaya: Journal of Asian Earth Sciences, v. 28, p. 385–408, doi:10.1016/j.jseaes.2005.09.012.

Godin, L., Brown, R.L., and Hanmer, S., 1999, High strain zone in the hanging wall of the Annapurna detachment, central Nepal Himalaya, *in* Macfarlane, A., Sorkhabi, R.B., and Quade, J., eds., Himalaya and Tibet: Mountain Roots to Mountain Tops: Geological Society of America Special Paper 328, p. 199–210, doi:10.1130/0-8137-2328-0.199.

Godin, L., Grujic, D., Law, R.D., and Searle, M.P., 2006, Channel flow, ductile extrusion and exhumation in continental collision zones: An introduction, *in* Law, R.D., et al., eds., Channel Flow, Ductile Extrusion and Exhumation in Continental Collision Zones: Geological Society of London Special Publication 268, p. 1–23, doi:10.1144/GSL.SP.2006.268.01.01.

Godin, L., Yakymchuk, C., and Harris, L.B., 2011, Himalayan hinterland-verging superstructure folds related to foreland-directed infrastructure ductile flow: Insights from centrifuge analogue modelling: Journal of Structural Geology, v. 33, p. 329–342, doi:10.1016/j.jsg.2010.09.005.

Gokul, A.R., 1983, Geological and Mineral Map of Bhutan: Hyderabad, India, Geological Survey of India Map Printing Division, scale 1:500,000, 1 sheet.

Greenwood, L.V., Argles, T.W., Parrish, R.R., Harris, N.B.W., and Warren, C., 2016, The geology and tectonics of central Bhutan: Journal of the Geological Society of London, v. 173, p. 352–369, doi:10.1144/jgs2015-031.

Grujic, D., Casey, M., Davidson, C., Hollister, L., Kundig, R., Pavlis, T.L., and Schmid, S., 1996, Ductile extrusion of the Higher Himalayan Crystalline in Bhutan: Evidence from quartz microfabrics: Tectonophysics, v. 260, p. 21–43, doi:10.1016/0040-1951(96)00074-1.

Grujic, D., Hollister, L.S., and Parrish, R.R., 2002, Himalayan metamorphic sequence as an orogenic channel: Insight from Bhutan: Earth and Planetary Science Letters, v. 198, p. 177–191, doi:10.1016/S0012-821X(02)00482-X.

Grujic, D., Warren, C.J., and Wooden, J.L., 2011, Rapid synconvergent exhumation of Miocene-aged lower and orogenic crust in the eastern Himalaya: Lithosphere, v. 3, p. 346–366, doi:10.1130/L154.1.

Guillope, M., and Poirier, J.P., 1979, Dynamic recrystallization during creep of single-crystalline halite: An experimental study: Journal of Geophysical Research, v. 84, p. 5557–5567, doi:10.1029/JB084iB10p05557.

Harrison, T.M., Ryerson, F.J., LeFort, P., Yin, A., Lovera, O., and Catlos, E.J., 1997, A late Miocene–Pliocene origin for the central Himalayan inverted metamorphism: Earth and Planetary Science Letters, v. 146, p. E1–E7, doi:10.1016/S0012-821X(96)00215-4.

He, D., Webb, A.A., Larson, K.P., Martin, A.J., and Schmitt, A.K., 2015, Extrusion vs. duplexing models of Himalayan mountain building 3: Duplexing dominates from the Oligocene to Present: International Geology Review, v. 57, p. 1–27, doi:10.1080/00206814.2014.986669.

He, D., Webb, A.A.G., Larson, K.P., and Schmitt, A.K., 2016, Extrusion vs. duplexing models of Himalayan mountain building 2: The South Tibet detachment at the Dadeldhura klippe: Tectonophysics, v. 667, p. 87–107, doi:10.1016/j.tecto.2015.11.014.

Henry, P., LePichon, X., and Goffe, B., 1997, Kinematic, thermal and petrological model of the Himalayas: Constraints related to metamorphism within the underthrust Indian crust and topographic elevation: Tectonophysics, v. 273, p. 31–56, doi:10.1016/S0040-1951(96)00287-9.

Herman, F., Copeland, P., Avouac, J.-P., Bollinger, L., Maheo, G., LeFort, P., Rai, S., Foster, D., Pecher, A., Stuwe, K., and Henry, P., 2010, Exhumation, crustal deformation, and thermal structure of the Nepal Himalaya derived from inversion of thermochronological and thermobarometric data and modeling of the topography: Journal of Geophysical Research, v. 115, p. B06407, doi:10.1029/2008JB006126.

Hodges, K.V., Parrish, R.R., Housch, T.B., Lux, D.R., Burchfiel, B.C., Royden, L.H., and Chen, Z., 1992, Simultaneous Miocene extension and shortening in the Himalayan orogen: Science, v. 258, p. 1466–1470, doi:10.1126/science.258.5087.1466.

Holdaway, M.J., 2000, Application of new experimental and garnet Margules data to the garnet-biotite geothermometer: The American Mineralogist, v. 85, p. 881–892, doi:10.2138/am-2000-0701.

Holland, T.J.B., and Powell, R., 2003, Activity-composition relations for phases in petrological calculations: An asymmetric multicomponent formulation: Contributions to Mineralogy and Petrology, v. 145, p. 492–501, doi:10.1007/s00410-003-0464-z.

Holland, T.J.B., and Powell, R., 2011, An improved and extended internally consistent thermodynamic dataset for phases of petrological interest, involving a new equation of state for solids: Journal of Metamorphic Geology, v. 29, p. 333–383, doi:10.1111/j.1525-1314.2010.00923.x.

Holyoke, C.W., and Tullis, J., 2006, Formation and maintenance of shear zones: Geology, v. 34, p. 105–108, doi:10.1130/G22116.1.

Jessup, M.J., Cottle, J.M., Searle, M.P., Law, R.D., Newell, D.L., Tracy, R.J., and Waters, D.J., 2008, P-T-t-D paths of Everest Series schist, Nepal: Journal of Metamorphic Geology, v. 26, p. 717–739, doi:10.1111/j.1525-1314.2008.00784.x.

Johnson, M.R.W., Oliver, G.J.H., Parrish, R.R., and Johnson, S.P., 2001, Synthrusting metamorphism, cooling, and erosion of the Himalayan Kathmandu complex, Nepal: Tectonics, v. 20, p. 394–415, doi:10.1029/2001TC900005.

Johnson, S.E., Lenferink, H.J., Price, N.A., Marsh, J.H., Koons, P.O., West, D.P., Jr., and Beane, R., 2009, Clast-based kinematic vorticity gauges: The effects of slip at matrix/clast interfaces: Journal of Structural Geology, v. 31, p. 1322–1339, doi:10.1016/j.jsg.2009.07.008.

Kellett, D.A., Grujic, D., and Erdmann, S., 2009, Miocene structural reorganization of the South Tibetan detachment, eastern Himalaya: Implications for continental collision: Lithosphere, v. 1, p. 259–281, doi:10.1130/L56.1.

Kellett, D.A., Grujic, D., Warren, C., Cottle, J., Jamieson, R., and Tenzin, T., 2010, Metamorphic history of a syn-convergent orogen-parallel detachment: The South Tibetan detachment system, Bhutan Himalaya: Journal of Metamorphic Geology, v. 28, p. 785–808, doi:10.1111/j.1525-1314.2010.00893.x.

Kellett, D.A., and Grujic, D., 2012, New insight into the South Tibetan detachment system: Not a single progressive deformation: Tectonics, v. 31, TC2007, doi:10.1029/2011TC002957.

Khanal, S., Robinson, D.M., Kohn, M.J., and Mandal, S., 2015, Evidence for a far-traveled thrust sheet in the Greater Himalayan thrust system, and an alternative model to building the Himalaya: Tectonics, v. 34, p. 31–52, doi:10.1002/2014TC003616.

Kohn, M.J., 2008, P-T-t data from central Nepal support critical taper and repudiate large-scale channel flow of the Greater Himalayan Sequence: Geological Society of America Bulletin, v. 120, p. 259–273, doi:10.1130/B26252.1.

Kohn, M.J., 2014, Himalayan metamorphism and its tectonic implications: Annual Review of Earth and Planetary Sciences, v. 42, p. 381–419, doi:10.1146/annurev-earth-060313-055005.

Larson, K.P., and Cottle, J.M., 2014, Midcrustal discontinuities and the assembly of the Himalayan midcrust: Tectonics, v. 33, p. 718–740, doi:10.1002/2013TC003452.

Larson, K.P., Ambrose, T.K., Webb, A.A.G., Cottle, J.M., and Shrestha, S., 2015, Reconciling Himalayan midcrustal discontinuities: The Main Central thrust system: Earth and Planetary Science Letters, v. 429, p. 139–146, doi:10.1016/j.epsl.2015.07.070.

Law, R.D., 2010, Moine thrust zone mylonites at the Stack of Glencoul: II—Results of vorticity analyses and their tectonic significance, *in* Law, R.D., Butler, R.W.H., Holdsworth, R., Krabbendam, M., and Strachan, R.A., eds., Continental Tectonics and Mountain Building—The

Legacy of Peach and Horne: Geological Society of London Special Publication 335, p. 579–602, doi:10.1144/SP335.24.

Law, R.D., 2014, Deformation thermometry based on quartz c-axis fabrics and recrystallization microstructures: A review: Journal of Structural Geology, v. 66, p. 129–161, doi:10.1016/j.jsg.2014.05.023.

Law, R.D., Searle, M.P., and Simpson, R.L., 2004, Strain, deformation temperatures and vorticity of flow at the top of the Greater Himalayan Slab, Everest Massif, Tibet: Journal of the Geological Society, v. 161, p. 305–320, doi:10.1144/0016-764903-047.

Law, R.D., Jessup, M.J., Searle, M.P., Francsis, M.K., Waters, D.J., and Cottle, J.M., 2011, Telescoping of isotherms beneath the South Tibetan Detachment System, Mount Everest Massif: Journal of Structural Geology, v. 33, p. 1569–1594, doi:10.1016/j.jsg.2011.09.004.

LeFort, P., 1975, Himalayas: The collided range. Present knowledge of the continental arc: American Journal of Science, v. 275-A, p. 1–44.

Lister, G.S., and Dornsiepen, U.F., 1982, Fabric transitions in the Saxony granulite terrain: Journal of Structural Geology, v, 4, p. 81–92.

Long, S., and McQuarrie, N., 2010, Placing limits on channel flow: Insights from the Bhutan Himalaya: Earth and Planetary Science Letters, v. 290, p. 375–390, doi:10.1016/j.epsl.2009.12.033.

Long, S., McQuarrie, N., Tobgay, T., Rose, C., Gehrels, G., and Grujic, D., 2011a, Tectonostratigraphy of the Lesser Himalaya of Bhutan: Implications for the along-strike stratigraphic continuity of the northern Indian margin: Geological Society of America Bulletin, v. 123, p. 1406–1426, doi:10.1130/B30202.1.

Long, S., McQuarrie, N., Tobgay, T., and Grujic, D., 2011b, Geometry and crustal shortening of the Himalayan fold-thrust belt, eastern and central Bhutan: Geological Society of America Bulletin, v. 123, p. 1427–1447, doi:10.1130/B30203.1.

Long, S., McQuarrie, N., Tobgay, T., and Hawthorne, J., 2011c, Quantifying internal strain and deformation temperature in the eastern Himalaya: Implications for the evolution of strain in thrust sheets: Journal of Structural Geology, v. 33, p. 579–608, doi:10.1016/j.jsg.2010.12.011.

Long, S.P., McQuarrie, N., Tobgay, T., Grujic, D., and Hollister, L., 2011d, Geologic map of Bhutan: The Journal of Maps, v. 2011, p. 184–192, 1:500,000-scale, doi:10.4113/jom.2011.1159.

Long, S.P., McQuarrie, N., Tobgay, T., Coutand, I., Cooper, F.J., Reiners, P.W., Wartho, J., and Hodges, K.V., 2012, Variable shortening rates in the eastern Himalayan thrust belt, Bhutan: Insights from multiple thermochronologic and geochronologic datasets tied to kinematic reconstructions: Tectonics, v. 31, TC5004, 23 p., doi:10.1029/2012TC003155.

Long, S.P., Gordon, S.M., Young, J.P., and Soignard, E., 2016, Temperature and strain gradients through Lesser Himalayan rocks and across the Main Central thrust, south-central Bhutan: Implications for transport-parallel stretching and inverted metamorphism: Tectonics, v. 35, p. 1863–1891, doi:10.1002/2016TC004242.

Mainprice, D.H., Bouchez, J.L., Blumenfeld, P., and Tubia, J.M., 1986, Dominant c slip in naturally-deformed quartz: Implications for dramatic plastic softening at high temperature: Geology, v. 14, p. 819–822, doi:10.1130/0091-7613(1986)14<819:DCSIND>2.0.CO;2.

Martin, A.J., 2016, A review of definitions of the Himalayan Main Central Thrust: International Journal of Earth Sciences, 15 p., doi:10.1007/s00531-016-1419-8.

Martin, A.J., DeCelles, P.G., Gehrels, G.E., Patchett, P.J., and Isachsen, C., 2005, Isotopic and structural constraints on the location of the Main Central thrust in the Annapurna Range, central Nepal Himalaya: Geological Society of America Bulletin, v. 117, p. 926–944, doi:10.1130/B25646.1.

Mattauer, M., 1986, Intracontinental subduction, crust-mantle décollement and crustal-stacking wedge in the Himalayas and other collision belts, *in* Coward, M.P., and Ries, A.C., eds., Collision Tectonics: Geological Society of London Special Publication 19, p. 37–50.

McQuarrie, N., Long, S.P., Tobgay, T., Nesbit, J.N., Gehrels, G., and Ducea, M., 2013, Documenting basin scale, geometry and provenance through detrital geochemical data: Lessons from the Neoproterozoic to Ordovician Lesser, Greater, and Tethyan Himalayan strata of Bhutan: Gondwana Research, v. 23, p. 1491–1510, doi:10.1016/j.gr.2012.09.002.

Means, W.D., 1994, Rotational quantities in homogeneous flow and the development of small-scale structures: Journal of Structural Geology, v. 17, p. 893–896.

Means, W.D., Hobbs, B.E., Lister, G.S., and Williams, P.F., 1980, Vorticity and noncoaxiality in progressive deformation: Journal of Structural Geology, v. 2, p. 371–378, doi:10.1016/0191-8141(80)90024-3.

Myrow, P.M., Hughes, N.C., Searle, M.P., Fanning, C.M., Peng, S.-C., and Parcha, S.K., 2009, Stratigraphic correlation of Cambrian–Ordovician deposits along the Himalaya: Implications for the age and nature of rocks in the Mount Everest region: Geological Society of America Bulletin, v. 121, p. 323–332, doi:10.1130/B26384.1.

Passchier, C.W., 1987, Stable positions of rigid objects in non-coaxial flow—A study in vorticity analysis: Journal of Structural Geology, v. 124, p. 211–222.

Passchier, C.W., and Trouw, R.A.J., 2005, Micro-tectonics, Second Edition: New York, Springer, 366 p.

Pêcher, A., 1991, The contact between the Higher Himalaya crystallines and the Tibetan sedimentary series: Miocene large-scale dextral shearing: Tectonics, v. 10, p. 587–598, doi:10.1029/90TC02655.

Poirier, J.P., and Nicolas, A., 1975, Deformation-induced recrystallization by progressive misorientation of subgrain-boundaries, with special reference to mantle peridotites: The Journal of Geology, v. 83, p. 707–720, doi:10.1086/628163.

Powell, C.M., and Conaghan, P.J., 1973, Plate tectonics and the Himalayas: Earth and Planetary Science Letters, v. 20, p. 1–12, doi:10.1016/0012-821X(73)90134-9.

Powell, R., and Holland, T.J.B., 1994, Optimal geothermometry and geobarometry: The American Mineralogist, v. 79, p. 120–133.

Rahl, J.M., Anderson, K.M., Brandon, M.T., and Fassoulas, C., 2005, Raman spectroscopic carbonaceous material thermometry of low-grade metamorphic rocks: Calibration and application to tectonic exhumation in Crete, Greece: Earth and Planetary Science Letters, v. 240, p. 339–354, doi:10.1016/j.epsl.2005.09.055.

Ramsay, J.G., 1967, Folding and fracturing of rocks: New York, McGraw-Hill, 560 p.

Ramsay, J.G., and Huber, M.I., 1983, Techniques of Modern Structural Geology, Vol. 1: Strain Analysis: London, Academic Press, 307 p.

Robinson, D.M., DeCelles, P.G., Garzione, C.N., Pearson, O.N., Harrison, T.M., and Catlos, E.J., 2003, Kinematic model for the Main Central thrust in Nepal: Geology, v. 31, p. 359–362, doi:10.1130/0091-7613(2003)031<0359:KMFTMC>2.0.CO;2.

Robinson, D.M., DeCelles, P.G., and Copeland, P., 2006, Tectonic evolution of the Himalayan thrust belt in western Nepal: Implications for channel flow models: Geological Society of America Bulletin, v. 118, p. 865–885, doi:10.1130/B25911.1.

Royden, L.H., 1993, The steady state thermal structure of eroding orogenic belts and accretionary prisms: Journal of Geophysical Research, v. 98, no. B3, p. 4487–4507, doi:10.1029/92JB01954.

Sanderson, D.J., 1982, Models of strain variation in nappes and thrust sheets: A review: Tectonophysics, v. 88, p. 201–233, doi:10.1016/0040-1951(82)90237-2.

Searle, M.P., and Rex, A.J., 1989, Thermal model for the Zanskar Himalaya: Journal of Metamorphic Geology, v. 7, p. 127–134, doi:10.1111/j.1525-1314.1989.tb00579.x.

Searle, M.P., Simpson, R.L., Law, R.D., Waters, D.J., and Parrish, R.R., 2002, Quantifying displacement on the South Tibetan detachment normal fault, Everest massif, and the timing of crustal thickening and uplift in the Himalaya and Tibet: Journal of Nepal Geological Society, v. 26, p. 1–6.

Searle, M., Simpson, R.L., Law, R.D., Parrish, R.R., and Waters, D.J., 2003, The structural geometry, metamorphic and magmatic evolution of the Everest massif, High Himalaya of Nepal–South Tibet: Journal of the Geological Society of London, v. 160, p. 345–366, doi:10.1144/0016-764902-126.

Searle, M.P., Law, R.D., Godin, L., Larson, K.P., Streule, M.J., Cottle, J.M., and Jessup, M.J., 2008, Defining the Himalayan Main Central thrust in Nepal: Journal of the Geological Society of London, v. 165, p. 523–534, doi:10.1144/0016-76492007-081.

Simpson, C., and DePaor, D.G., 1993, Strain and kinematic analysis in general shear zones: Journal of Structural Geology, v. 15, p. 1–20, doi:10.1016/0191-8141(93)90075-L.

Soucy La Roche, R., Godin, L., Cottle, J.M., and Kellett, D.A., 2016, Direct shear fabric dating constrains early Oligocene onset of the South Tibetan detachment in the western Nepal Himalaya: Geology, v. 44, p. 403–406, doi:10.1130/G37754.1.

Stipp, M., Stunitz, H., Heilbronner, R., and Schmid, S.M., 2002, The eastern Tonale fault zone: A 'natural laboratory' for crystal plastic deformation over a temperature range from 250° to 700°C: Journal of Structural Geology, v. 24, p. 1861–1884, doi:10.1016/S0191-8141(02)00035-4.

Stocklin, J., 1980, Geology of Nepal and its regional frame: Journal of the Geological Society of London, v. 137, p. 1–34, doi:10.1144/gsjgs.137.1.0001.

Swapp, S.M., and Hollister, L.S., 1991, Inverted metamorphism within the Tibetan slab of Bhutan: Evidence for a tectonically transported heat source: Canadian Mineralogist, v. 29, p. 1019–1041.

Tangri, S.K., and Pande, A.C., 1995, Tethyan Sequence, *in* Bhargava, O.N., ed., The Bhutan Himalaya: A Geological Account: Geological Society of India Special Publication 39, p. 109–142.

Tikoff, B., and Fossen, H., 1993, Simultaneous pure and simple shear: The unifying deformation matrix: Tectonophysics, v. 217, p. 267–283, doi:10.1016/0040-1951(93)90010-H.

Tikoff, B., and Fossen, H., 1995, The limitations of three-dimensional kinematic vorticity analysis: Journal of Structural Geology, v. 17, p. 1771–1784, doi:10.1016/0191-8141(95)00069-P.

Tobgay, T., McQuarrie, N., Long, S., Kohn, M.J., and Corrie, S., 2012, The age and rate of displacement along the Main Central Thrust in the western Bhutan Himalaya: Earth and Planetary Science Letters, v. 319–320, p. 146–158, doi:10.1016/j.epsl.2011.12.005.

Treagus, S.H., and Treagus, J.E., 2002, Studies of strain and rheology of conglomerates: Journal of Structural Geology, v. 24, p. 1541–1567, doi:10.1016/S0191-8141(01)00162-6.

Tullis, J., and Wenk, H.-R., 1994, Effect of muscovite on the strength and lattice preferred orientations of experimentally deformed quartz aggregates: Materials Science and Engineering, ser. A, v. 175, p. 209–220, doi:10.1016/0921-5093(94)91060-X.

Upreti, B.N., and LeFort, P., 1999, Lesser Himalayan crystalline nappes of Nepal: Problem of their origin, *in* Macfarlane, A., Quade, J., and Sorkhabi, R., eds., Himalaya and Tibet: Mountain Roots to Mountain Tops: Geological Society of America Special Paper 328, p. 225–238, doi:10.1130/0-8137-2328-0.225.

Urai, J.L., Means, W.D., and Lister, G.S., 1986, Dynamic recrystallization of minerals, *in* Hobbs, B.E., and Heard, H.C., eds., Mineral and Rock Deformation: Laboratory Studies: Washington, D.C., American Geophysical Union Monograph v. 36, p. 161–199, doi:10.1029/GM036p0161.

van Hinsbergen, D.J.J., Lippert, P.C., Dupont-Nivet, G., McQuarrie, N., Doubrovine, P.V., Spakman, W., and Torsvik, T.H., 2012, Greater India Basin hypothesis and a two-stage Cenozoic collision between India and Asia: Proceedings of the National Academy of Sciences of the United States of America, v. 109, p. 7659–7664, doi:10.1073/pnas.1117262109.

Warren, C.J., Grujic, D., Kellett, D.A., Cottle, J., Jamieson, R.A., and Ghalley, K.S., 2011, Probing the depths of the India-Asia collision: U-Th-Pb monazite chronology of granulites from NW Bhutan: Tectonics, v. 30, doi:10.1029/2010TC002738.

Warren, C.J., Grujic, D., Cottle, J., and Rogers, N.W., 2012, Constraining cooling histories: Rutile and titanite chronology and diffusion modeling in NW Bhutan: Journal of Metamorphic Geology, v. 30, p. 113–130, doi:10.1111/j.1525-1314.2011.00958.x.

Webb, A.A.G., 2013, Preliminary balanced palinspastic reconstruction of Cenozoic deformation across the Himachal Himalaya (northwestern India): Geosphere, v. 9, p. 572–587, doi:10.1130/GES00787.1.

Webb, A.A.G., Yin, A., Harrison, M.T., Celerier, J., and Burgess, P.W., 2007, The leading edge of the Greater Himalayan crystalline complex revealed in the NW Indian Himalaya: Implications for the evolution of the Himalayan orogen: Geology, v. 35, p. 955–958, doi:10.1130/G23931A.1.

Webb, A.A.G., Schmitt, A.K., He, D., and Weigand, E.L., 2011, Structural and geochronological evidence for the leading edge of the Greater Himalayan crystalline complex in the central Nepal Himalaya: Earth and Planetary Science Letters, v. 304, p. 483–495, doi:10.1016/j.epsl.2011.02.024.

White, S., 1977, Geological significance of recovery and recrystallization processes in quartz: Tectonophysics, v. 39, p. 143–170, doi:10.1016/0040-1951(77)90093-2.
Whitney, D.L., and Evans, B.W., 2010, Abbreviations for names of rock-forming minerals: The American Mineralogist, v. 95, p. 185–187, doi:10.2138/am.2010.3371.
Wu, C., Nelson, K.D., Wortman, G., Samson, S.D., Yongjun, Y., Jixiang, L., Kidd, W.S.F., and Edwards, M.A., 1998, Yadong cross structure and South Tibetan detachment in the east central Himalaya (89°–90°E): Tectonics, v. 17, p. 28–45, doi:10.1029/97TC03386.
Xypolias, P., Spanos, D., Chatzaras, V., Kokkalas, S., and Koukouvelas, I., 2010, Vorticity of flow in ductile thrust zones: Examples from the Attico-Cycladic Massif (Internal Hellenides, Greece), *in* Law, R.D., Butler, R.W.H., Holdsworth, R., Krabbendam, M., and Strachan, R.A., eds., Continental Tectonics and Mountain Building: Geological Society of London Special Publication, v. 335, p. 687–714, doi:10.1144/SP335.28.
Yin, A., 2006, Cenozoic tectonic evolution of the Himalayan orogen as constrained by along-strike variation of structural geometry, exhumation history, and foreland sedimentation: Earth-Science Reviews, v. 76, p. 1–131, doi:10.1016/j.earscirev.2005.05.004.
Yin, A., and Harrison, T.M., 2000, Geologic evolution of the Himalayan-Tibetan orogen: Annual Review of Earth and Planetary Sciences, v. 28, p. 211–280, doi:10.1146/annurev.earth.28.1.211.
Yonkee, A., 2005, Strain patterns within part of the Willard thrust sheet, Idaho-Wyoming-Utah thrust belt: Journal of Structural Geology, v. 27, p. 1315–1343, doi:10.1016/j.jsg.2004.06.014.
Yonkee, W.A., Czeck, D.M., Nachbor, A.C., Barszewski, C., Pantone, S., Balgord, E.A., and Johnson, K.R., 2013, Strain accumulation and fluid-rock interaction in a naturally deformed diamictite, Willard thrust system, Utah (USA): Implications for crustal rheology and strain softening: Journal of Structural Geology, v. 50, p. 91–118, doi:10.1016/j.jsg.2012.10.012.
Zeiger, K., Gordon, S.M., Long, S.P., Kylander-Clark, A.R.C., Agustsson, K., and Penfold, M., 2015, Timing and conditions of metamorphism and melt crystallization in Greater Himalayan rocks, eastern and central Bhutan: Insight from U-Pb zircon and monazite geochronology and trace-element analyses: Contributions to Mineralogy and Petrology, v. 169, art. 47, 19 p., doi:10.1007/s00410-015-1143-6.

MANUSCRIPT RECEIVED 14 FEBRUARY 2017
REVISED MANUSCRIPT RECEIVED 28 APRIL 2017
MANUSCRIPT ACCEPTED 8 JUNE 2017

Printed in the USA